IEEE Access
Multidisciplinary | Rapid Review | Open Access Journal

Received August 8, 2021, accepted August 30, 2021, date of publication September 1, 2021, date of current version September 13, 2021.

Digital Object Identifier 10.1109/ACCESS.2021.3109621

Hierarchical Volt-VAR Optimization Framework Considering Voltage Control of Smart Electric Vehicle Charging Stations Under Uncertainty

PANGGAH PRABAWA, (Student Member, IEEE), AND DAE-HYUN CHOI, (Member, IEEE)
School of Electrical and Electronics Engineering, Chung-Ang University, Seoul 156-756, South Korea

Corresponding author: Dae-Hyun Choi (dhchoi@cau.ac.kr)

This work was supported in part by the Basic Science Research Program through the National Research Foundation of Korea (NRF) funded by the Ministry of Education under Grant 2020R1F1A1049314, and in part by the Ministry of Science and ICT (MSIT), South Korea, through the Information Technology Research Center (ITRC) support program, supervised by the Institute for Information & Communications Technology Planning & Evaluation (IITP), under Grant IITP-2021-2018-0-01799.

ABSTRACT Smart electric vehicle charging stations (EVCSs) equipped with distributed energy resources (DERs), such as photovoltaic (PV) systems and energy storage systems (ESSs), are promising entities for maintaining voltage quality in power distribution networks through voltage regulation using the smart inverters of DERs. This study proposes a hierarchical Volt-VAR optimization (VVO) framework that reflects the voltage regulation capability of smart EVCSs, which consists of global and local voltage control stages. At the global stage, smart inverters of EVCSs cooperate with conventional voltage regulators, such as an on-load tap changer (OLTC) and capacitor banks (CBs)), and smart inverters of PV systems to minimize the total active power losses and voltage deviations along with the determination of optimal parameters for local droop control functions of the smart inverters. At the local stage, smart inverters of EVCSs and PV systems quickly mitigate local voltage violations using dynamically varying local droop control functions with their optimal parameters calculated from the global stage. Under uncertainties in PV generation outputs and driving patterns of electric vehicle users, the deterministic optimization-based VVO problem at the global stage is reformulated into the chance-constrained optimization-based VVO problem. A simulation study was performed in an IEEE 33-bus distribution system with an OLTC, CBs, PV systems, and smart EVCSs. The results demonstrate the effectiveness of the proposed framework in terms of total active power loss/voltage deviation, optimized local droop control function, and probability level of chance constraints.

INDEX TERMS Volt-VAR optimization, local voltage control, smart inverter, electric vehicle charging station, chance-constrained optimization.

NOMENCLATURE

The main notations used throughout this paper are summarized here. Hat symbols represent estimates of true parameter values. Other undefined symbols are explained in the text.

A. ABBREVIATIONS

CB	Capacitor bank
CCO	Chanced constrained optimization
DER	Distributed energy resource
DO	Deterministic optimization
EV	Electric vehicle
ESS	Energy storage system
EVCS	Electric vehicle charging station
OLTC	On-load tap changer
PV	Photovoltaic
SOC	State of charge
VVO	Volt-VAR optimization

B. SETS

$\mathcal{T}$	Set of scheduling horizon.
$\mathcal{L}$	Set of lines in distribution network.
$\mathcal{N}$	Set of nodes in distribution network.
$\mathcal{N}^{\mathrm{SI}}$	Set of nodes with smart inverters in distribution network.
$\mathcal{N}^{\mathrm{PV}}$	Set of nodes with PV systems in distribution network.
$\mathcal{N}^{\mathrm{ESS}}$	Set of nodes with ESSs in distribution network.

The associate editor coordinating the review of this manuscript and approving it for publication was Reinaldo Tonkoski.

$\mathcal{N}^{\text{EVCS}}$	Set of nodes with EVCSs in distribution network.
$\mathcal{E}_i$	Set of EVs connected to node i with EVCS.
$\mathcal{Y}_{e,i}$	Set of all possible driving pattern realizations for EV e of EVCS at node i.

C. VARIABLES

$P^{\text{loss}}_{ij,t}$	Active power flow loss of line ij at time t.
$P(Q)^{\text{line}}_{ij,t}$	Active (reactive) power flow of line ij at time t.
$P(Q)^{\text{EVCS}}_{i,t}$	Injected/absorbed active (reactive) power from EVCS at node i and time t.
$P^{\text{ESS,c(d)}}_{i,t}$	Active charging (discharging) power for ESS of EVCS at node i and time t.
$P^{\text{EV,c}}_{e,i,t}$	Active charging power for EV e of EVCS at node i and time t.
$SOC^{\text{ESS}}_{i,t}$	SOC for ESS of EVCS at node i and time t.
$SOC^{\text{EV}}_{e,i,t}$	SOC for EV e of EVCS at node i and time t.
$Q^{\text{PV(CB)}}_{i,t}$	Reactive power capability of PV system (CB) at node i and time t.
$V_{i,t}$	Voltage magnitude at node i and time t.
$Q^{*}_{i}(V_{i,t})$	Reactive power of smart inverter at node i and time t with respect to $V_{i,t}$ in Q-V curve.
Tap^{OLTC}_{t}	Integer variable for determining a tap position of OLTC at time t.
$b^{\text{CB}}_{i,t}$	Binary variable for determining a switch status of CB at node i and time t.
$b^{\text{ESS}}_{i,t}$	Binary variable for determining a charging or discharging status for ESS of EVCS at node i and time t.
$b^{\text{ESS}}_{e,i,t}$	Binary variable for determining a charging status for EV e of EVCS at node i and time t.
$b_{e,y}$	Binary variable for realization y of the possible driving patterns for EV e.
$V^{\text{q}}_{i,\{3,4\}}$	Controlled parameters of Q-V curve for smart inverter at node i.
$\alpha^{\text{q}}_{i,t,k}$	Continuous auxiliary variables of Q-V curve for smart inverter at node i and time t ($k = 1 \sim 6$).
$\gamma^{\text{q}}_{i,t,k}$	Binary auxiliary variables of Q-V curve for smart inverter at node i and time t ($k = 1 \sim 6$).
$\varphi^{\text{q,min}}_{i}$, $\varphi^{\text{q,max}}_{i}$	Integer auxiliary variables for linearization of $\alpha^{\text{q}}_{i,t,3}V^{\text{q}}_{i,3}$ and $\alpha^{\text{q}}_{i,t,4}V^{\text{q}}_{i,4}$ at node i and time t.
$\kappa^{\text{q,min}}_{i,m}$, $\kappa^{\text{q,max}}_{i,m}$	Binary auxiliary variables for binary expansion linearization at node i ($m = 1 \sim 5$).
$\delta^{\text{q,min}}_{i,t,m}$, $\delta^{\text{q,max}}_{i,t,m}$	Continuous auxiliary variables for big-M linearization at node i and time t ($m = 1 \sim 5$).

D. PARAMETERS

$\widehat{P}(\widehat{Q})^{\text{load}}_{i,t}$	Predicted active (reactive) power demand at node i and time t.
$\widehat{P}^{\text{PV}}_{i,t}$	Predicted active power output of PV system at node i and time t.
$P^{\text{ESS,c(d),max}}_{i}$	Maximum charging (discharging) active power for ESS of EVCS at node i.
$P^{\text{EV,c,max}}_{e,i}$	Maximum charging active power for EV e of EVCS at node i.
$P^{\text{EV,d}}_{e,i,t}$	Discharging active power for EV e of EVCS at node i and time t.
$P^{\text{EV,d}}_{e,y,t}$	Discharging active power for EV e on realization y at node i and time t.
$SOC^{\text{ESS,min(max)}}_{i}$	Minimum (maximum) SOC limit for ESS of EVCS at node i.
$SOC^{\text{EV,min(max)}}_{e,i}$	Minimum (maximum) SOC limit for EV e of EVCS at node i.
SOC^{ESS}_{i,t_0}	Initial SOC for ESS of EVCS at node i and time $t = t_0$.
$SOC^{\text{EV}}_{e,i,t_0}$	Initial SOC for EV e of EVCS at node i and time $t = t_0$.
$E^{\text{ESS,cap}}_{i}$	Maximum battery capacity for ESS of EVCS at node i.
$E^{\text{EV,cap}}_{e,i}$	Maximum battery capacity for EV e of EVCS at node i.
$\eta^{\text{EV,c}}_{e,i}$	Charging efficiency for EV e of EVCS at node i.
$\eta^{\text{ESS,c(d)}}_{i}$	Charging (discharging) efficiency for ESS of EVCS at node i.
$b^{\text{EV}}_{e,i,t}$	Binary charging status for EV e of EVCS at node i and time t.
$b^{\text{EV}}_{e,y,t}$	Binary charging status for EV e of EVCS on driving pattern realization y at node i and time t
$V^{\text{min(max)}}_{\text{thr}}$	Minimum (maximum) threshold of voltage magnitude.
$V^{\text{min(max)}}$	Minimum (maximum) limit of voltage magnitude.
$r(x)_{ij}$	Resistance (reactance) of distribution line ij.
V^{nom}	Nominal voltage magnitude (1 p.u.).
a^{OLTC}	Step size of change in OLTC tap position.
$Q^{\text{CB,nom}}_{i}$	Nominal reactive power of CB at node i.
$Q^{\text{PV,max}}_{i}$	Maximum reactive power capacity of PV system at node i.

$S_i^{\mathrm{PV,max}}$	Maximum apparent power capacity of PV system at node i.
$Q_i^{\mathrm{EVCS,max}}$	Maximum reactive power capacity of EVCS at node i.
$S_i^{\mathrm{EVCS,max}}$	Maximum apparent power capacity of EVCS at node i.
$V_{i,\{1,2,5,6\}}^{\mathrm{q}}$	Fixed parameters of Q-V curve for smart inverter at node i.
v^{step}	Step size of voltage increment in Q-V curve.
Q_k^{q}	Breaking points in Q-V curve ($k = 1 \sim 6$).
$\mu(\sigma)_{i,t}^{\mathrm{PV,err}}$	Mean (standard deviation) of the prediction error of PV generation output at node i and time t.
$\psi_{e,y}$	Probability of realization y of all possible driving patterns for EV e.
β	Probability level in the chance constraints.

I. INTRODUCTION

As power distribution networks are integrated with various distributed energy resources (DERs), such as solar photovoltaic (PV) systems, energy storage systems (ESSs), and electric vehicles (EVs), passive power distribution networks are transformed into active power distribution networks [1]. DERs enhance the reliability and resiliency of active distribution networks [2], [3] and provide network self-healing capability [4], efficient demand response and load balancing using smart meters [5], [6], and economic energy market regulation [7], [8]. However, fluctuations in the DER power outputs (e.g., intermittent PV generation output due to cloud movements and uncertain charging behavior of EV users) may lead to unstable grid conditions, thereby yielding voltage violations owing to reverse power flow [9], [10].

A smart inverter connected to DERs is a crucial power electronic device for maintaining a stable operation of the power distribution system. Smart inverter converts the direct current output of DERs into alternating current, and provides grid support functions such as voltage/frequency regulation and power factor control via advanced communication and control [11]. To maintain a normal voltage level in the active power distribution network, smart inverters are generally used as new voltage regulating devices in a centralized Volt-VAR optimization (VVO) (one of the main applications for distribution management systems) that determines optimal nodal voltage magnitudes through the coordination of traditional voltage regulators such as on-load tap changers (OLTCs) and capacitor banks (CBs) and the smart inverters of DERs [12]. Furthermore, the centralized VVO is integrated with smart inverter-based local voltage control for smart inverters to rapidly inject or absorb the reactive power of DERs by using their local droop control function to mitigate local voltage violations [13].

EVs are being increasingly deployed in active power distribution networks to resolve environmental concerns about gasoline engine vehicles (e.g., greenhouse gas and carbon emissions) and improve the efficiency of grid energy management by providing vehicle-to-grid applications that support ancillary services such as voltage and frequency regulation [14]. More recently, to support efficient charging services to EV users, maximize the profit of electric vehicle charging station (EVCS) owners, and maintain a stable grid operation, a traditional EVCSs are being transformed into smart EVCSs equipped with PV systems and ESSs [15], [16]. Evidently, smart inverters of PV systems and ESSs installed in smart EVCSs hold promise for maintaining high-quality voltage levels in active power distribution networks by exploiting their voltage regulation capability. This study propose a novel hierarchical VVO framework that reflects the voltage regulation capability of smart inverters of EVCSs to minimize the total active power loss and voltage deviation in active power distribution networks. To achieve this objective, the proposed VVO framework consists of global and local control stages. The global control stage includes two tasks: i) optimal operation scheduling of smart inverters for EVCSs/PV systems and voltage regulators and ii) calculation of optimal local droop control functions of smart inverters. The local control stage involves the operation of smart inverters based on the local droop control functions optimized from the global control stage to quickly mitigate local voltage violations.

Since the pioneering study [17] on Volt-VAR control, which reduces the network power loss and maintains a normal voltage profile by exploiting voltage regulators, many studies have developed optimization-based VVO algorithms through different approaches: advanced branch-and-cut [18], particle swarm optimization [19], genetic algorithm-based NSGA-II [20], and mixed-integer linear programming (MILP) and mixed-integer nonlinear programming (MINLP) to achieve conservation voltage reduction [21]. Various robust VVO methods against the uncertainty in PV power generation output were proposed. In [22], a rule-based approach for decentralized control of the reactive power of a PV system was presented using chance-constrained linear programming to reduce voltage violations owing to the fluctuations of PV power output. A two-level chance constrained VVO method considering the uncertainty in both PV active power and load demand was developed [23] to minimize the total active power loss using OLTC, step voltage regulators, and smart inverters of PV systems. In [24], a coordination framework between VVO and home energy management system using a chance-constrained optimization method was proposed in which uncertainties in PV active power output and temperature were considered, and the total electricity bill for electricity consumers was reduced while maintaining an acceptable voltage level in unbalanced distribution systems. Furthermore, ESSs were integrated into VVO to minimize the total power loss of unbalanced three-phase distribution systems using second-order cone

programming and semidefinite programming [25], and to reduce the total cost of energy purchased from the distribution substation and distributed generators using mixed-integer second-order programming [26]. In [27], a distributed voltage regulation problem considering storage-capable loads, such as plug-in EVs, was formulated to reduce the network loss by dispatching active and reactive power for distributed generators and plug-in hybrid EVs. An online distributed model predictive control method was developed in [28] in which the optimal EV charging process under uncertainty of EV arrival is carried out in realistic operating conditions of power distribution systems, including active/reactive power flow and bus voltage constraints.

The aforementioned optimization-based VVO methods may not conduct optimal voltage regulation in situations where unexpected and sudden local voltage changes occur due to intermittent DER power output because OLTCs and CBs are not sufficiently fast to regulate voltage. To address this challenge, a local voltage control method based on a piecewise linear droop control curve was proposed. Using the Volt-VAR curve [29], namely the Q-V curve, which is one of the droop control curves, DER inverters absorb or inject reactive power of the DER from or to the grid based on their voltage measurements to rapidly mitigate local voltage violations. Various hierarchical VVO frameworks were presented in which smart inverters using the Q-V curve quickly conduct reactive power dispatch of their DERs in fast scheduling intervals at the local stage, while the OLTCs and CBs regulate the voltage in a slow scheduling interval at the global stage. In [30], a three-stage VVO method was developed in which the OLTC and CBs are scheduled in 1 h period at the first stage, the smart inverters are scheduled in a 15 min period at the second stage, and the local voltage control based on the Q-V curve is executed by smart inverters in a second period at the third stage. In [31], a two-level conservation voltage reduction method was presented to achieve energy saving with a lower voltage profile in which the OLTC and CBs reduce the voltage profile at the global level, and the smart inverters of PV systems and ESSs help to maintain a lower voltage profile using the proposed Q-V curves at the local level. In [32], a power factor-based droop control curve for the smart inverter of a PV system was proposed to mitigate voltage violations and excessive tap operations of step voltage regulators with line drop compensation. More recently, as opposed to the aforementioned local control strategies using the Q-V curve with fixed parameters, novel optimization methods that adjust the parameters in the Q-V curve were presented; the simulation results showed that dynamically changing Q-V curves can further reduce voltage deviations and active power losses. They include a centralized method for determining the optimal parameters of the Q-V curve for the smart inverter of a PV system [33] and soft open point [34], and a distributed method for determining the optimal parameters of the Q-V curve for the smart inverter of a PV system using the alternating direction method of multipliers algorithm [35].

However, no previous studies on the development of hierarchical VVO methods considered smart inverters of smart EVCSs as voltage regulators in both the global and local control stages. Furthermore, under uncertain environments associated with PV generation output and EV driving patterns, no performance analysis for the voltage regulation capability of such smart inverters was conducted. A novelty of this study is that, under the aforementioned uncertainties, the smart inverters of smart EVCSs perform the global VVO process by cooperating with the OLTC, CBs and smart inverters of PV systems to reduce the total active power loss and voltage deviation, while the local voltage control process using the optimized Q-V curves of the smart inverters is carried out to quickly mitigate local voltage violations. Therefore, the main contributions of this study can be summarized as follows:

- We propose a hierarchical VVO framework where the total active power losses and voltage deviations are minimized through the coordination of smart inverters of EVCSs and conventional voltage regulating devices (OLTC and CBs) along with smart inverters of stand-alone PV systems.
- The proposed VVO framework consists of two stages as shown in Fig. 1. At the global stage, the VVO algorithm aims to reduce the total active power losses and voltage deviations by conducting two tasks: i) scheduling optimal operations of the OLTC, CBs, and smart inverters of EVCSs and PV systems, and ii) calculating optimal parameters for the Q-V curves of the smart inverters. At the local stage, the smart inverters of EVCS and PV systems are executed to quickly mitigate local voltage violations using the optimized Q-V curves embedded with the parameters that are calculated at the global stage.
- We formulate a deterministic optimization (DO)-based VVO algorithm as a MILP model in which the nonlinear constraints for the reactive power capability of EVCSs and the Q-V curve, along with the nonlinear objective function for voltage deviation are linearized.
- To reflect uncertainty in the PV generation outputs and driving patterns of the EV users, we reformulate the DO-based VVO algorithm into the chance-constrained optimization (CCO)-based VVO algorithm by transforming deterministic constraints for nodal voltage magnitude and state of charge (SOC) of ESSs for EVCSs and EVs into the chance constraints.

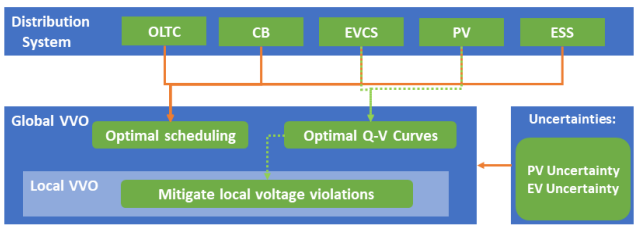

FIGURE 1. Architecture of the proposed two-stage hierarchical VVO framework under uncertainty.

- Simulation results demonstrate the effectiveness of the proposed DO- and CCO-based VVO methods integrated with optimized Q-V curves and the robustness of the CCO-based VVO approach against uncertainties in terms of total active power loss and voltage deviation.

The remainder of this paper is organized as follows. Section II presents a two-stage DO-based VVO model that includes the smart inverters of EVCSs. A CCO-based VVO model that reflects the uncertainty of PV generation outputs and driving patterns of EVs is described in Section III. Section IV reports the simulation results for the proposed framework. Finally, conclusions are drawn in Section V.

II. TWO-STAGE DO-BASED VVO PROBLEM

Traditionally, the VVO problem involves two voltage control stages. At the global stage, an acceptable voltage level along the distribution feeder is maintained through the coordination of an OLTC, CBs, and the smart inverters of DERs as an optimization problem. When local voltage violations occur suddenly owing to intermittent PV power generation, the smart inverters of DERs are rapidly controlled based on their local droop control curve (i.e., Q-V curve) to mitigate the voltage violations at the local stage. In this study, the smart inverters of a PV system and an ESS that are connected to the EVCS are used as the voltage regulators to solve the VVO problem at both the global and local control stages.

A. GLOBAL CONTROL STAGE

1) OBJECTIVE FUNCTION

Let us denote the set of nodes as $\mathcal{N} = \mathcal{N}^{\mathrm{SI}} \cup (\mathcal{N}^{\mathrm{SI}})^c$; $\mathcal{N}^{\mathrm{SI}}$ represents the set of nodes with smart inverters. The set of nodes $\mathcal{N}^{\mathrm{SI}}$ is decomposed into three sets: $\mathcal{N}^{\mathrm{PV}}$ for PV systems, $\mathcal{N}^{\mathrm{ESS}}$ for ESSs, and $\mathcal{N}^{\mathrm{EVCS}}$ for EVCSs.

For each node $i,\ j \in \mathcal{N}$ and each distribution line $ij \in \mathcal{L}$ with scheduling period $t \in \mathcal{T}$, the objective of the VVO at the global stage is to minimize the following weighted multi-objective function in terms of ω_1 and ω_2:

$$\min \sum_{t\in\mathcal{T}} \left(\omega_1 \sum_{ij\in\mathcal{L}} P^{\mathrm{loss}}_{ij,t} + \omega_2 \sum_{i\in\mathcal{N}} \left| V_{i,t} - V^{\mathrm{nom}} \right| \right). \quad (1)$$

In (1), the first term denotes the total active power loss for all lines during the scheduling horizon, and the active power loss is expressed as

$$P^{\mathrm{loss}}_{ij,t} = r_{ij} \left[\left(P^{\mathrm{line}}_{ij,t} \right)^2 + \left(Q^{\mathrm{line}}_{ij,t} \right)^2 \right]. \quad (2)$$

The second term in (1) represents the total deviation of voltages from the nominal voltage ($V^{\mathrm{nom}} = 1.0$ p.u.) for all nodes during the scheduling horizon when $V_{i,t}$ is larger than $V^{\max}_{\mathrm{thr}}$ or smaller than $V^{\min}_{\mathrm{thr}}$. The nonlinear second term can be linearized using the auxiliary variable $\Delta V_{i,t}$ as follows:

$$\Delta V_{i,t} = \left| V_{i,t} - V^{\mathrm{nom}} \right| \quad (3)$$

$$\Delta V_{i,t} \geq V_{i,t} - V^{\max}_{\mathrm{thr}} \quad (4)$$

$$\Delta V_{i,t} \geq V^{\min}_{\mathrm{thr}} - V_{i,t} \quad (5)$$

$$\Delta V_{i,t} \geq 0. \quad (6)$$

The following subsections illustrate the equality and inequality constraints for the VVO problem at the global stage.

2) DISTRIBUTION SYSTEM OPERATING CONSTRAINTS

For each node $h,\ i,\ j \in \mathcal{N}$, (7) and (8) represent the active and reactive power balance constraints at bus i, respectively. Equation (9) expresses the voltage drop between nodes i and j. Equation (10) denotes the substation voltage, which is determined by varying the OLTC tap position with a fixed step size a^{OLTC}. The OLTC tap position Tap^{OLTC}_t has an integer value that normally ranges from -16 to 16. Equation (11) represents the reactive power supplied by the CB for node i at scheduling period t. In (11), a binary decision variable, $b^{\mathrm{CB}}_{i,t}$, determines the switch status of the CB (i.e., "1" for ON and "0" for OFF), and $Q^{\mathrm{CB,nom}}_i$ is the size of the CB. Equation (12) limits the range of the allowable voltage magnitude for node i at scheduling period t with minimum ($V^{\min}$) and maximum ($V^{\max}$) values. In this study, $V^{\min}$ and $V^{\max}$ are set to 0.9 p.u. and 1.1 p.u., respectively.

$$\sum_{hi\in\mathcal{L}} P^{\mathrm{line}}_{hi,t} + P^{\mathrm{EVCS}}_{i,t} + \widehat{P}^{\mathrm{PV}}_{i,t} = \sum_{ij\in\mathcal{L}} P^{\mathrm{line}}_{ij,t} + \widehat{P}^{\mathrm{load}}_{i,t} \quad (7)$$

$$\sum_{hi\in\mathcal{L}} Q^{\mathrm{line}}_{hi,t} + Q^{\mathrm{EVCS}}_{i,t} + Q^{\mathrm{PV}}_{i,t} + Q^{\mathrm{CB}}_{i,t} = \sum_{ij\in\mathcal{L}} Q^{\mathrm{line}}_{ij,t} + \widehat{Q}^{\mathrm{load}}_{i,t} \quad (8)$$

$$V_{j,t} = V_{i,t} - \left(\frac{r_{ij} P^{\mathrm{line}}_{ij,t} + x_{ij,t} Q^{\mathrm{line}}_{ij,t}}{V^{\mathrm{nom}}} \right) \quad (9)$$

$$V_{1,t} = V^{\mathrm{nom}} + a^{\mathrm{OLTC}} Tap^{\mathrm{OLTC}}_t \quad (10)$$

$$Q^{\mathrm{CB}}_{i,t} = b^{\mathrm{CB}}_{i,t} Q^{\mathrm{CB,nom}}_i \quad (11)$$

$$V^{\min} \leq V_{i,t} \leq V^{\max}. \quad (12)$$

3) EV CONSTRAINTS

For each EV $e \in \mathcal{E}_i$ at EVCS $i \in \mathcal{N}^{\mathrm{EVCS}}$, (13) expresses the operation of the cumulated SOC for the EV battery in terms of charging and discharging power, i.e., $P^{\mathrm{EV,c}}_{e,i,t'}$ and $P^{\mathrm{EV,d}}_{e,i,t'}$, charging efficiency $\eta^{\mathrm{EV,c}}_{e,i}$, battery capacity $E^{\mathrm{EV,cap}}_{e,i}$, and initial SOC $SOC^{\mathrm{EV}}_{e,i,t_0}$ of EV e. Note that the charging power $P^{\mathrm{EV,c}}_{e,i,t'}$ is a decision variable, whereas the discharging power $P^{\mathrm{EV,d}}_{e,i,t'}$ is a parameter. The capacity constraint of the SOC of the EV battery is presented in (14) with which the safe charging operation of the EV can be maintained. Equation (15) expresses the constraint on the charging power of the EV battery where $b^{\mathrm{EV}}_{e,i,t}$ is the binary decision variable that determines the status of EV charging (i.e., "1" for charging

and "0" for non-charging).

$$SOC_{e,i,t}^{\mathrm{EV}} = \sum_{t'=t_0}^{t} \left(\frac{P_{e,i,t'}^{\mathrm{EV,c}} \eta_{e,i}^{\mathrm{EV,c}}}{E_{e,i}^{\mathrm{EV,cap}}} - \frac{P_{e,i,t'}^{\mathrm{EV,d}}}{E_{e,i}^{\mathrm{EV,cap}}} \right) + SOC_{e,i,t_0}^{\mathrm{EV}} \tag{13}$$

$$SOC_{e,i}^{\mathrm{EV,min}} \leq SOC_{e,i,t}^{\mathrm{EV}} \leq SOC_{e,i}^{\mathrm{EV,max}} \tag{14}$$

$$0 \leq P_{e,i,t}^{\mathrm{EV,c}} \leq b_{e,i,t}^{\mathrm{EV}} P_{e,i}^{\mathrm{EV,c,max}}. \tag{15}$$

4) ESS CONSTRAINTS

For each ESS $i \in \mathcal{N}^{\mathrm{ESS}}$, (16) illustrates the operation of the cumulated SOC for the ESS in terms of charging and discharging power, i.e., $P_{i,t'}^{\mathrm{ESS,c}}$ and $P_{i,t'}^{\mathrm{ESS,d}}$, charging and discharging efficiency, i.e., $\eta_i^{\mathrm{ESS,c}}$ and $\eta_i^{\mathrm{ESS,d}}$, battery capacity $E_i^{\mathrm{ESS,cap}}$, and initial SOC $SOC_{i,t_0}^{\mathrm{ESS}}$ of ESS i. The capacity of the SOC of the ESS is limited according to (17) because the overcharging and undercharging of the ESS may have a detrimental impact on the ESS lifetime. Equations (18) and (19) provide the constraints on the charging and discharging power of the ESS, where the binary decision variable $b_{i,t}^{\mathrm{ESS}}$ ensures that the charging and discharging of the ESS are mutually exclusive at time t (i.e., "1" for charging and "0" for discharging).

$$SOC_{i,t}^{\mathrm{ESS}} = \sum_{t'=t_0}^{t} \left(\frac{P_{i,t'}^{\mathrm{ESS,c}} \eta_i^{\mathrm{ESS,c}}}{E_i^{\mathrm{ESS,cap}}} - \frac{P_{i,t'}^{\mathrm{ESS,d}}}{\eta_i^{\mathrm{ESS,d}} E_i^{\mathrm{ESS,cap}}} \right) + SOC_{i,t_0}^{\mathrm{ESS}} \tag{16}$$

$$SOC_i^{\mathrm{ESS,min}} \leq SOC_{i,t}^{\mathrm{ESS}} \leq SOC_i^{\mathrm{ESS,max}} \tag{17}$$

$$0 \leq P_{i,t}^{\mathrm{ESS,c}} \leq b_{i,t}^{\mathrm{ESS}} P_i^{\mathrm{ESS,c,max}} \tag{18}$$

$$0 \leq P_{i,t}^{\mathrm{ESS,d}} \leq \left(1 - b_{i,t}^{\mathrm{ESS}}\right) P_i^{\mathrm{ESS,d,max}} \tag{19}$$

5) PV CONSTRAINTS

For each PV system $i \in \mathcal{N}^{\mathrm{PV}}$, the reactive power output of the PV system is limited by the predicted active power output $\widehat{P}_{i,t}^{\mathrm{PV}}$ and the maximum apparent power $S_i^{\mathrm{PV,max}}$ of the PV system in (20). Equation (21) represents the normalized PV reactive power output associated with the time-varying voltage magnitude in the local control droop curve of the PV system, which is described in Section II-B.

$$\left(Q_{i,t}^{\mathrm{PV}}\right)^2 + \left(\widehat{P}_{i,t}^{\mathrm{PV}}\right)^2 \leq \left(S_i^{\mathrm{PV,max}}\right)^2 \tag{20}$$

$$\frac{Q_{i,t}^{\mathrm{PV}}}{Q_i^{\mathrm{PV,max}}} = Q_i^*(V_{i,t}). \tag{21}$$

6) EVCS CONSTRAINTS

We consider a smart EVCS $i \in \mathcal{N}^{\mathrm{EVCS}}$ that is equipped with a PV system and an ESS. Equation (22) expresses the net power consumption of the EVCS, i.e., the difference between the total charging power ($\sum_{e \in \mathcal{E}_i} P_{e,i,t}^{\mathrm{EV,c}}$) of EVs at EVCS i with the charging power ($P_{i,t}^{\mathrm{ESS,c}}$) of the ESS and the predicted PV active power output ($\widehat{P}_{i,t}^{\mathrm{PV}}$) with the discharging power ($P_{i,t}^{\mathrm{ESS,d}}$) of the ESS. The reactive power output of the EVCS is bounded by its net power consumption $P_{i,t}^{\mathrm{EVCS}}$ and its maximum apparent power $S_i^{\mathrm{EVCS,max}}$ in (23), which determines the allowable active and reactive powers of the EVCS to prevent its overcapacity. Similar to the constraint (21), the relationship between the reactive power of the EVCS and the time-varying voltage magnitude in the local control droop curve of the EVCS is expressed in (24).

$$P_{i,t}^{\mathrm{EVCS}} = \sum_{e \in \mathcal{E}_i} P_{e,i,t}^{\mathrm{EV,c}} + P_{i,t}^{\mathrm{ESS,c}} - \widehat{P}_{i,t}^{\mathrm{PV}} - P_{i,t}^{\mathrm{ESS,d}} \tag{22}$$

$$\left(Q_{i,t}^{\mathrm{EVCS}}\right)^2 + \left(P_{i,t}^{\mathrm{EVCS}}\right)^2 \leq \left(S_i^{\mathrm{EVCS,max}}\right)^2 \tag{23}$$

$$\frac{Q_{i,t}^{\mathrm{EVCS}}}{Q_i^{\mathrm{EVCS,max}}} = Q_i^*(V_{i,t}). \tag{24}$$

In contrast to the linear constraint (20) of the reactive power capacity for the PV system, (23) defines a nonlinear constraint with two quadratic decision variables. The nonlinear constraint can be linearized using the polygon-based realization method [36] as follows. Using the radius of the polygon S_i^{EVCS} in (25), where n, which is set to 6, denotes the number of sides of the polygon, three linear inequality constraints (26)–(28) are obtained:

$$S_i^{\mathrm{EVCS}} = S_i^{\mathrm{EVCS,max}} \sqrt{(2\pi/n)/\sin(2\pi/n)} \tag{25}$$

$$-\sqrt{3}\left(P_{i,t}^{\mathrm{EVCS}} + S_i^{\mathrm{EVCS}}\right) \leq Q_{i,t}^{\mathrm{EVCS}} \leq -\sqrt{3}\left(P_{i,t}^{\mathrm{EVCS}} - S_i^{\mathrm{EVCS}}\right) \tag{26}$$

$$-\frac{\sqrt{3}}{2} S_i^{\mathrm{EVCS}} \leq Q_{i,t}^{\mathrm{EVCS}} \leq \frac{\sqrt{3}}{2} S_i^{\mathrm{EVCS}} \tag{27}$$

$$\sqrt{3}\left(P_{i,t}^{\mathrm{EVCS}} - S_i^{\mathrm{EVCS}}\right) \leq Q_{i,t}^{\mathrm{EVCS}} \leq \sqrt{3}\left(P_{i,t}^{\mathrm{EVCS}} + S_i^{\mathrm{EVCS}}\right). \tag{28}$$

B. LOCAL CONTROL STAGE

The smart inverters of the PV system and EVCS at node $i \in \mathcal{N}^{\mathrm{PV}} \cup \mathcal{N}^{\mathrm{EVCS}}$ initiate local voltage control process when a voltage violation is detected using the local voltage measurements collected by their inverter. Local voltage control can be conducted based on the dynamically varying Q-V curve shown in Fig. 2, where the reactive power outputs of the PV system and EVCS are locally injected or absorbed according to the values of the collected voltage measurements in the Q-V curve.

As shown in Fig. 2, the Q-V curve for the smart inverter i consists of six break points: four fixed points, $V_1^{\mathrm{q}} = 0.8$ p.u., $V_2^{\mathrm{q}} = 0.9$ p.u., $V_5^{\mathrm{q}} = 1.1$ p.u., and $V_6^{\mathrm{q}} = 1.2$ p.u., and two varying points, $V_{i,3}^{\mathrm{q}}$ and $V_{i,4}^{\mathrm{q}}$, at node $i \in \mathcal{N}^{\mathrm{PV}} \cup \mathcal{N}^{\mathrm{EVCS}}$. Note that the optimal Q-V curve can be constructed according to the optimal values of $V_{i,3}^{\mathrm{q}}$ and $V_{i,4}^{\mathrm{q}}$, which can

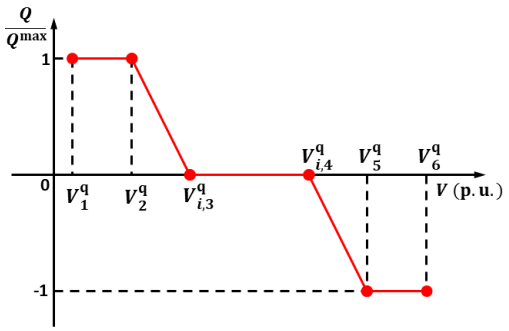

FIGURE 2. Dynamic Q-V curve for the smart inverters of the PV system and EVCS at node i.

be written as [35]

$$Q_i^*(V_{i,t}) = \begin{cases} 1, & V_{i,t} \in \left[V_1^{\mathrm{q}}, V_2^{\mathrm{q}}\right) \\ \dfrac{1}{V_2^{\mathrm{q}} - V_{i,3}^{\mathrm{q}}} V_{i,t} + \dfrac{V_{i,3}^{\mathrm{q}}}{V_{i,3}^{\mathrm{q}} - V_2^{\mathrm{q}}}, & V_{i,t} \in \left[V_2^{\mathrm{q}}, V_{i,3}^{\mathrm{q}}\right) \\ 0, & V_{i,t} \in \left[V_{i,3}^{\mathrm{q}}, V_{i,4}^{\mathrm{q}}\right) \\ \dfrac{1}{V_{i,4}^{\mathrm{q}} - V_5^{\mathrm{q}}} V_{i,t} + \dfrac{V_{i,4}^{\mathrm{q}}}{V_5^{\mathrm{q}} - V_{i,4}^{\mathrm{q}}}, & V_{i,t} \in \left[V_{i,4}^{\mathrm{q}}, V_5^{\mathrm{q}}\right) \\ -1, & V_{i,t} \in \left[V_5^{\mathrm{q}}, V_6^{\mathrm{q}}\right]. \end{cases} \tag{29}$$

Using the approach reported in [33], the aforementioned piecewise Q-V curve can be embedded as linear constraints into the VVO problem at the global control stage. With additional continuous variables, i.e., $\alpha_{i,t,k}^{\mathrm{q}}$ $(k = 1 \sim 6)$, and binary variables, i.e., $\gamma_{i,t,k}^{\mathrm{q}}$ $(k = 1 \sim 5)$, (29) can be reformulated as

$$V_{i,t} = \sum_{k=1}^{6} \alpha_{i,t,k}^{\mathrm{q}} V_k^{\mathrm{q}} \tag{30}$$

$$Q_i^*(V_{i,t}) = \sum_{k=1}^{6} \alpha_{i,t,k}^{\mathrm{q}} Q_k^{\mathrm{q}} \tag{31}$$

$$\alpha_{i,t,1}^{\mathrm{q}} \le \gamma_{i,t,1}^{\mathrm{q}}, \quad \alpha_{i,t,6}^{\mathrm{q}} \le \gamma_{i,t,5}^{\mathrm{q}} \tag{32}$$

$$\alpha_{i,t,k}^{\mathrm{q}} \le \gamma_{i,t,k}^{\mathrm{q}} + \gamma_{i,t,k-1}^{\mathrm{q}}, \quad k = 2,\ 3,\ 4,\ 5 \tag{33}$$

$$\alpha_{i,t,k}^{\mathrm{q}} \ge 0. \tag{34}$$

The voltage magnitude at node $i \in \mathcal{N}^{\mathrm{PV}} \cup \mathcal{N}^{\mathrm{EVCS}}$ is expressed in (30). The controlled amount of reactive power injection or absorption is shown in (31) where Q_k^{q} represents the y-position of the six breaking points in the Q-V curve with $Q_k^{\mathrm{q}} = \{1, 1, 0, 0, -1, -1\}$ $(k = 1 \sim 6)$. Equations (32)–(34) are used to form the linear functions corresponding to the piecewise linear curves in (29). However, (30) is still a nonlinear constraint because it includes the terms of the multiplication of two variables, $\alpha_{i,t,3}^{\mathrm{q}} V_{i,3}^{\mathrm{q}}$ and $\alpha_{i,t,4}^{\mathrm{q}} V_{i,4}^{\mathrm{q}}$. To linearize the nonlinear constraint, a binary expansion method along with auxiliary integer variables, $\varphi_i^{\mathrm{q,min}}$ and $\varphi_i^{\mathrm{q,max}}$, is used as follows [35]:

$$\alpha_{i,t,3}^{\mathrm{q}} V_{i,3}^{\mathrm{q}} = \alpha_{i,t,3}^{\mathrm{q}} \left(V_2^{\mathrm{q}} + v^{\mathrm{step}} \varphi_i^{\mathrm{q,min}}\right) \tag{35}$$

$$0 \le \varphi_i^{\mathrm{q,min}} \le \frac{V_5^{\mathrm{q}} - V_2^{\mathrm{q}}}{v^{\mathrm{step}}} \tag{36}$$

$$\alpha_{i,t,4}^{\mathrm{q}} V_{i,4}^{\mathrm{q}} = \alpha_{i,t,4}^{\mathrm{q}} \left(V_2^{\mathrm{q}} + v^{\mathrm{step}} \varphi_i^{\mathrm{q,max}}\right) \tag{37}$$

$$0 \le \varphi_i^{\mathrm{q,max}} \le \frac{V_5^{\mathrm{q}} - V_2^{\mathrm{q}}}{v^{\mathrm{step}}} \tag{38}$$

$$\varphi_i^{\mathrm{q,min}} \le \varphi_i^{\mathrm{q,max}}. \tag{39}$$

The variables $V_{i,3}^{\mathrm{q}}$ and $V_{i,4}^{\mathrm{q}}$ are incremented by the parameter v^{step} in (35), (36) and (37), (38), respectively, where v^{step} modifies the upper bound of integer variables $\varphi_i^{\mathrm{q,min}}$ and $\varphi_i^{\mathrm{q,max}}$. Equation (39) enables $V_{i,3}^{\mathrm{q}}$ and $V_{i,4}^{\mathrm{q}}$ to meet at a point. To further linearize the nonlinear terms $\alpha_{i,t,3}^{\mathrm{q}} \varphi_i^{\mathrm{q,min}}$ in (35) and $\alpha_{i,t,4}^{\mathrm{q}} \varphi_i^{\mathrm{q,max}}$ in (37), the binary expansion method is first applied to $\varphi_i^{\mathrm{q,min}}$ and $\varphi_i^{\mathrm{q,max}}$ as follows:

$$\varphi_i^{\mathrm{q,min}} = \sum_{m=1}^{5} 2^{m-1} \kappa_{i,m}^{\mathrm{q,min}} \tag{40}$$

$$\varphi_i^{\mathrm{q,max}} = \sum_{m=1}^{5} 2^{m-1} \kappa_{i,m}^{\mathrm{q,max}}. \tag{41}$$

After substituting (40) and (41) into (35) and (37) and linearizing them using the big-M method with the auxiliary variables $\delta_{i,t,m}^{\mathrm{q,min}} = \alpha_{i,t,3}^{\mathrm{q}} \kappa_{i,m}^{\mathrm{q,min}}$ and $\delta_{i,t,m}^{\mathrm{q,max}} = \alpha_{i,t,4}^{\mathrm{q}} \kappa_{s,m}^{\mathrm{q,max}}$, the following inequality constraints are obtained:

$$\alpha_{i,t,3}^{\mathrm{q}} - \left(1 - \kappa_{i,m}^{\mathrm{q,min}}\right) M \le \delta_{i,t,m}^{\mathrm{q,min}} \le \alpha_{i,t,3}^{\mathrm{q}} \tag{42}$$

$$0 \le \delta_{i,t,m}^{\mathrm{q,min}} \le \kappa_{i,m}^{\mathrm{q,min}} M \tag{43}$$

$$\alpha_{i,t,4}^{\mathrm{q}} - \left(1 - \kappa_{i,m}^{\mathrm{q,max}}\right) M \le \delta_{i,t,m}^{\mathrm{q,max}} \le \alpha_{i,t,4}^{\mathrm{q}} \tag{44}$$

$$0 \le \delta_{i,t,m}^{\mathrm{q,max}} \le \kappa_{i,m}^{\mathrm{q,max}} M. \tag{45}$$

Then, $\delta_{i,t,m}^{\mathrm{q,min}}$ and $\delta_{i,t,m}^{\mathrm{q,max}}$ are substituted into (35) and (37), which in turn become

$$\alpha_{i,t,3}^{\mathrm{q}} V_{i,3}^{\mathrm{q}} = V_2^{\mathrm{q}} \alpha_{i,t,3}^{\mathrm{q}} + v^{\mathrm{step}} \sum_{m=1}^{5} 2^{m-1} \delta_{i,t,m}^{\mathrm{q,min}} \tag{46}$$

$$\alpha_{i,t,4}^{\mathrm{q}} V_{i,4}^{\mathrm{q}} = V_2^{\mathrm{q}} \alpha_{i,t,4}^{\mathrm{q}} + v^{\mathrm{step}} \sum_{m=1}^{5} 2^{m-1} \delta_{i,t,m}^{\mathrm{q,max}}. \tag{47}$$

In summary, the DO-based VVO problem considering the construction of the optimal Q-V curve for the smart inverters of the PV system and EVCS can be formulated as the following optimization problem:

$$\min \sum_{t \in \mathcal{T}} \left(\omega_1 \sum_{ij \in \mathcal{L}} P_{ij,t}^{\mathrm{loss}} + \omega_2 \sum_{i \in \mathcal{N}} \left| V_{i,t} - V^{\mathrm{nom}} \right| \right)$$
$$\text{s.t Eqn. (2), (4)–(22), (24)–(28), (30)–(34),}$$
$$\text{(36), (38)–(47).} \tag{48}$$

III. CCO-BASED VVO MODEL UNDER PV AND EV UNCERTAINTIES

We consider two types of uncertain sources with prediction errors for i) the PV active power generation output, and ii) the EV user's driving pattern. The uncertainty of the PV generation output influences the constraints of the DO-based VVO model, including the voltage magnitude limit given by (9) and (12) via the active power flow expressed by (7) and the constraint of the SOC limit for the EVCS expressed by (16) and (17). The uncertainty of the EV user's driving pattern impacts the constraints of the SOC of the EV battery and the charging limits for the EV in (13)–(15). The derivations of the chance constraints for the PV and EV uncertainties are presented in Sections III-A and III-B, respectively.

A. PV UNCERTAINTY

1) CHANCE CONSTRAINTS FOR VOLTAGE MAGNITUDE LIMIT

The PV power generation output $P_{i,t}^{\mathrm{PV}}$ is modeled in terms of the predicted PV output $\widehat{P}_{i,t}^{\mathrm{PV}}$ and its prediction error $P_{i,t}^{\mathrm{PV,err}}$ [37]:

$$P_{i,t}^{\mathrm{PV}} = \widehat{P}_{i,t}^{\mathrm{PV}} + \widehat{P}_{i,t}^{\mathrm{PV}} P_{i,t}^{\mathrm{PV,err}}. \tag{49}$$

Using the voltage drop equation (9), the chance constraints on the upper and lower limits (12) of the voltage magnitude for node i at time t are expressed as

$$\Pr\left\{\begin{array}{l} V^{\min} \le V_{h,t} - \left(r_{hi}P_{hi,t}^{\mathrm{line}} + x_{hi}Q_{hi,t}^{\mathrm{line}}\right) \\ V_{h,t} - \left(r_{hi}P_{hi,t}^{\mathrm{line}} + x_{hi}Q_{hi,t}^{\mathrm{line}}\right) \le V^{\max} \end{array}\right. \ge \beta. \tag{50}$$

where, with a probability of at least β, the voltage magnitude $V_{i,t}$ should be maintained within the range $[V^{\min}, V^{\max}]$.

Let us assume that $\Delta_{hi,t}^{\mathrm{V,min}} = V^{\min} - [V_{h,t} - (r_{hi}P_{hi,t}^{\mathrm{line}} + x_{hi}Q_{hi,t}^{\mathrm{line}})]$ and $\Delta_{hi,t}^{\mathrm{V,max}} = [V_{h,t} - (r_{hi}P_{hi,t}^{\mathrm{line}} + x_{hi}Q_{hi,t}^{\mathrm{line}})] - V^{\max}$. Then, (50) is rewritten as follows:

$$\Pr\left\{\begin{array}{l} \Delta_{hi,t}^{\mathrm{V,min}} \le 0 \\ \Delta_{hi,t}^{\mathrm{V,max}} \le 0 \end{array}\right. \ge \beta. \tag{51}$$

Using the expression $P_{hi,t}^{\mathrm{line}}$ in (7) and the expression of the PV generation output in (49), $\Delta_{hi,t}^{\mathrm{V,max}}$ can be rewritten as

$$\begin{aligned} \Delta_{hi,t}^{\mathrm{V,max}} = V_{h,t} - \Big[r_{hi}\Big(& \sum_{ij\in\mathcal{L}} P_{ij,t}^{\mathrm{line}} - \widehat{P}_{i,t}^{\mathrm{load}} - P_{i,t}^{\mathrm{EVCS}} \\ & - (\widehat{P}_{i,t}^{\mathrm{PV}} + \widehat{P}_{i,t}^{\mathrm{PV}} P_{i,t}^{\mathrm{PV,err}})\Big) + x_{hi}Q_{hi,t}^{\mathrm{line}}\Big]. \end{aligned} \tag{52}$$

The prediction error $P_{i,t}^{\mathrm{PV,err}}$ of the PV generation output is assumed to follow a normal distribution with mean $\mu_{i,t}^{\mathrm{PV,err}}$ and variance $(\sigma_{i,t}^{\mathrm{PV,err}})^2$. Then, the mean $\mu_{hi,t}^{\Delta^{\mathrm{V,max}}}$ and variance $(\sigma_{hi,t}^{\Delta^{\mathrm{V,max}}})^2$ for $\Delta_{hi,t}^{\mathrm{V,max}}$ are respectively calculated as

$$\begin{aligned} \mu_{hi,t}^{\Delta^{\max}} = V_{h,t} - \Big[r_{hi}\Big(& \sum_{ij\in\mathcal{L}} P_{ij,t}^{\mathrm{line}} - P_{i,t}^{\mathrm{load}} - P_{i,t}^{\mathrm{G}} - P_{i,t}^{\mathrm{EVCS}} \\ & - \widehat{P}_{i,t}^{\mathrm{PV}}(1 + \mu_{i,t}^{\mathrm{PV,err}})\Big) + x_{hi}Q_{hi,t}^{\mathrm{line}}\Big] - V^{\max} \end{aligned} \tag{53}$$

$$(\sigma_{hi,t}^{\Delta^{\max}})^2 = r_{hi}^2 (\widehat{P}_{i,t}^{\mathrm{PV}})^2 (\sigma_{i,t}^{\mathrm{PV,err}})^2. \tag{54}$$

Using the results in (53) and (54) and the inverse cumulative distribution function $\Phi^{-1}(\cdot)$ of the standard normal distribution with zero mean and unit variance, the chance constraint for $\Delta_{hi,t}^{\max}$ can be rewritten as the following analytical constraint:

$$\mu_{hi,t}^{\Delta^{\max}} \le \sigma_{hi,t}^{\Delta^{\max}} \Phi^{-1}(\beta). \tag{55}$$

The chance constraint for $\Delta_{hi,t}^{\min}$ can also be derived in the same manner as the analytical constraint.

2) CHANCE CONSTRAINTS FOR SOC LIMIT OF ESS IN EVCS

The prediction error of the generation output of the PV system installed at the smart EVCS may result in an incorrect SOC level of the ESS in the EVCS because the PV generation output is preferentially charged to the ESS. To reflect the impact of the PV prediction error on the SOC of the ESS in the EVCS, $P_{i,t'}^{\mathrm{ESS,c}}$ in the deterministic SOC constraint (16) is replaced by the sum of $P_{i,t'}^{\mathrm{ESS,c}}$ and $\widehat{P}_{i,t'}^{\mathrm{PV}} P_{i,t'}^{\mathrm{PV,err}}$, and the deterministic constraints (16) and (17) are formulated as the following chance constraints:

$$\Pr\left\{\begin{array}{l} SOC_{i,t}^{\mathrm{ESS,min}} \le \sum_{t'=t_0}^{t}\left[\dfrac{(P_{i,t'}^{\mathrm{ESS,c}} + \widehat{P}_{i,t'}^{\mathrm{PV}} P_{i,t'}^{\mathrm{PV,err}})\eta_i^{\mathrm{ESS,c}}}{E_i^{\mathrm{ESS,cap}}} - \dfrac{P_{i,t'}^{\mathrm{ESS,d}}}{\eta_i^{\mathrm{ESS,d}} E_i^{\mathrm{ESS,cap}}}\right] + SOC_{i,t_0}^{\mathrm{ESS}} \\ \sum_{t'=t_0}^{t}\left[\dfrac{(P_{i,t'}^{\mathrm{ESS,c}} + \widehat{P}_{i,t}^{\mathrm{PV}} P_{i,t}^{\mathrm{PV,err}})\eta_i^{\mathrm{ESS,c}}}{E_i^{\mathrm{ESS,cap}}} - \dfrac{P_{i,t}^{\mathrm{ESS,d}}}{\eta_i^{\mathrm{ESS,d}} E_i^{\mathrm{ESS,cap}}}\right] + SOC_{i,t_0}^{\mathrm{ESS}} \\ \le SOC_{i,t}^{\mathrm{ESS,max}} \end{array}\right. \ge \beta. \tag{56}$$

Defining

$$\begin{aligned} \Delta_{i,t}^{\mathrm{ESS,min}} = SOC_{i,t}^{\mathrm{ESS,min}} - \sum_{t'=t_0}^{t}\Bigg[& \frac{(P_{i,t'}^{\mathrm{ESS,c}} + \widehat{P}_{i,t}^{\mathrm{PV}} P_{i,t}^{\mathrm{PV,err}})\eta_i^{\mathrm{ESS,c}}}{E_i^{\mathrm{ESS,cap}}} \\ & - \frac{P_{i,t'}^{\mathrm{ESS,d}}}{\eta_i^{\mathrm{ESS,d}} E_i^{\mathrm{ESS,cap}}}\Bigg] - SOC_{i,t_0}^{\mathrm{ESS}} \end{aligned} \tag{57}$$

$$\begin{aligned} \Delta_{i,t}^{\mathrm{ESS,max}} = \sum_{t'=t_0}^{t}\Bigg[& \frac{(P_{i,t'}^{\mathrm{ESS,c}} + \widehat{P}_{i,t}^{\mathrm{PV}} P_{i,t}^{\mathrm{PV,err}})\eta_i^{\mathrm{ESS,c}}}{E_i^{\mathrm{ESS,cap}}} \\ & - \frac{P_{i,t'}^{\mathrm{ESS,d}}}{\eta_i^{\mathrm{ESS,d}} E_i^{\mathrm{ESS,cap}}}\Bigg] + SOC_{i,t_0}^{\mathrm{ESS}} - SOC_{i,t}^{\mathrm{ESS,max}}, \end{aligned} \tag{58}$$

and using the results in (57) and (58), the chance constraint (56) can be rewritten as

$$\Pr\left\{\begin{array}{l} \Delta_{i,t}^{\mathrm{ESS,min}} \le 0 \\ \Delta_{i,t}^{\mathrm{ESS,max}} \le 0 \end{array}\right. \ge \beta. \tag{59}$$

Similar to the derivation of the chance constraints of the voltage magnitude limits associated with PV uncertainty, the

chance constraint for $\Delta_{i,t}^{\mathrm{ESS,max}}$ is reformulated as the following analytical constraint:

$$\mu_{i,t}^{\Delta^{\mathrm{ESS,max}}} \leq \sigma_{i,t}^{\Delta^{\mathrm{ESS,max}}} \Phi^{-1}(\beta) \tag{60}$$

where the mean $\mu_{i,t}^{\Delta^{\mathrm{ESS,max}}}$ and variance $(\sigma_{i,t}^{\Delta^{\mathrm{ESS,max}}})^2$ for $\Delta_{i,t}^{\mathrm{ESS,max}}$ are respectively calculated as

$$\mu_{i,t}^{\Delta^{\mathrm{ESS,max}}} = \sum_{t'=t_0}^{t} \left[\frac{(P_{i,t'}^{\mathrm{ESS,c}} + \widehat{P}_{i,t}^{\mathrm{PV}} \mu_{i,t}^{\mathrm{PV,err}}) \eta_i^{\mathrm{ESS,c}}}{E_i^{\mathrm{ESS,cap}}} - \frac{P_{i,t'}^{\mathrm{ESS,d}}}{\eta_i^{\mathrm{ESS,d}} E_i^{\mathrm{ESS,cap}}} \right] + SOC_{i,t_0}^{\mathrm{ESS}} - SOC_{i,t}^{\mathrm{ESS,max}} \tag{61}$$

$$(\sigma_{i,t}^{\Delta^{\mathrm{ESS,max}}})^2 = \sum_{t'=t_0}^{t} \left(\frac{\widehat{P}_{i,t}^{\mathrm{PV}} \eta_i^{\mathrm{ESS,c}}}{E_i^{\mathrm{ESS,cap}}} \right)^2 (\sigma_{i,t}^{\mathrm{PV,err}})^2. \tag{62}$$

Using the same procedure followed above, the chance constraint for $\Delta_{i,t}^{\mathrm{ESS,min}}$ can also be readily reformulated as an analytical constraint.

B. EV UNCERTAINTY

The chance constraints on the upper and lower limits (13)–(15) of the SOC and charging power for EV e at EVCS i and time t are expressed as [38]

$$\Pr \left\{ \begin{array}{l} SOC_{e,i}^{\mathrm{EV,min}} \leq \sum_{t'=t_0}^{t} \left(\frac{P_{e,i,t'}^{\mathrm{EV,c}} \eta_{e,i}^{\mathrm{EV,c}}}{E_{e,i}^{\mathrm{EV,cap}}} - \frac{P_{e,i,t'}^{\mathrm{EV,d}}}{E_{e,i}^{\mathrm{EV,cap}}} \right) + SOC_{e,i,t_0}^{\mathrm{EV}} \\ \sum_{t'=t_0}^{t} \left(\frac{P_{e,i,t'}^{\mathrm{EV,c}} \eta_{e,i}^{\mathrm{EV,c}}}{E_{e,i}^{\mathrm{EV,cap}}} - \frac{P_{e,i,t'}^{\mathrm{EV,d}}}{E_{e,i}^{\mathrm{EV,cap}}} \right) + SOC_{e,i,t_0}^{\mathrm{EV}} \\ \leq SOC_{e,i}^{\mathrm{EV,max}} \\ 0 \leq P_{e,i,t}^{\mathrm{EV,c}} \leq b_{e,i,t}^{\mathrm{EV}} P_{e,i}^{\mathrm{EV,c,max}} \end{array} \right. \geq \beta. \tag{63}$$

In (63), the uncertainty of the driving pattern for the EV user is associated with the stochastic parameters $P_{e,i,t'}^{\mathrm{EV,d}}$ and $b_{e,i,t}^{\mathrm{EV}}$; in general, these parameters do not follow a normal distribution. Furthermore, $b_{e,i,t}^{\mathrm{EV}}$ is a stochastic parameter with a binary value. To transform the above chance constraints into analytical constraints, we generate the realizations of various driving patterns associated with the parameters $P_{e,y,t'}^{\mathrm{EV,d}}$ and $b_{e,y,t}^{\mathrm{EV}}$ along with the probability $\psi_{e,y}$ of each realization $y \in \mathcal{Y}_{e,i}$ [38]. Using an auxiliary binary variable $b_{e,y}$ for each realization y, the chance constraints (63) can be rewritten as

$$SOC_{e,i}^{\mathrm{EV,min}} \leq \sum_{t'=t_0}^{t} \left(\frac{P_{e,i,t'}^{\mathrm{EV,c}} \eta_{e,i}^{\mathrm{EV,c}}}{E_{e,i}^{\mathrm{EV,cap}}} - \frac{P_{e,y,t'}^{\mathrm{EV,d}}}{E_{e,i}^{\mathrm{EV,cap}}} \right) + SOC_{e,i,t_0}^{\mathrm{EV}} + b_{e,y} \sum_{t'=t_0}^{t} \frac{P_{e,y,t'}^{\mathrm{EV,d}}}{E_{e,i}^{\mathrm{EV,cap}}} \tag{64}$$

$$\sum_{t'=t_0}^{t} \left(\frac{P_{e,i,t'}^{\mathrm{EV,c}} \eta_{e,i}^{\mathrm{EV,c}}}{E_{e,i}^{\mathrm{EV,cap}}} - \frac{P_{e,y,t'}^{\mathrm{EV,d}}}{E_{e,i}^{\mathrm{EV,cap}}} \right) + SOC_{e,i,t_0}^{EV} \leq SOC_{e,i}^{\mathrm{EV,max}} + b_{e,y} \sum_{t'=t_0}^{t} \left(\frac{P_{e,i}^{\mathrm{EV,c,max}}}{E_{e,i}^{\mathrm{EV,cap}}} - \frac{P_{e,y,t'}^{\mathrm{EV,d}}}{E_{e,i}^{\mathrm{EV,cap}}} \right) \tag{65}$$

$$P_{e,i,t}^{\mathrm{EV,c}} \leq b_{e,y,t}^{\mathrm{EV}} P_{e,i}^{\mathrm{EV,c,max}} + b_{e,y} P_{e,i}^{\mathrm{EV,c,max}} \tag{66}$$

$$\sum_{y \in \mathcal{Y}_{e,i}} (\psi_{e,y} b_{e,y}) \leq 1 - \beta. \tag{67}$$

To further constrict the constraints (64)–(67) along with the reduction in the number of binary decision variables, the set $\mathcal{Y}_{e,i}$ of possible driving realizations for EV e at EVCS i can be divided into the following two subsets: i) $\mathcal{Y}_{e,i}^{+} = \{y \in \mathcal{Y}_{e,i} : \psi_{e,y} > 1 - \beta\}$ and ii) $\mathcal{Y}_{e,i}^{-} = \{y \in \mathcal{Y}_{e,i} : \psi_y \leq 1 - \beta$. Based on the two subsets $\mathcal{Y}_{e,i}^{+}$ and $\mathcal{Y}_{e,i}^{-}$ ($y_1 \in \mathcal{Y}_{e,i}^{+}$, $y_2 \in \mathcal{Y}_{e,i}^{-}$), the constraints (64)–(67) are reformulated as

$$SOC_{e,i}^{\mathrm{EV,min}} \leq \sum_{t'=t_0}^{t} \left(\frac{P_{e,i,t}^{\mathrm{EV,c}} \eta_{e,i}^{\mathrm{EV,c}}}{E_{e,i}^{\mathrm{EV,cap}}} - \frac{P_{e,y_1,t}^{\mathrm{EV,d}}}{E_{e,i}^{\mathrm{EV,cap}}} \right) + SOC_{e,i,t_0}^{\mathrm{EV}} \tag{68}$$

$$\sum_{t'=t_0}^{t} \left(\frac{P_{e,i,t}^{\mathrm{EV,c}} \eta_{e,i}^{\mathrm{EV,c}}}{E_{e,i}^{\mathrm{EV,cap}}} - \frac{P_{e,y_1,t}^{\mathrm{EV,d}}}{E_{e,i}^{\mathrm{EV,cap}}} \right) + SOC_{e,i,t_0}^{\mathrm{EV}} \leq SOC_{e,i}^{\mathrm{EV,max}} \tag{69}$$

$$P_{e,i,t}^{\mathrm{EV,c}} \leq b_{e,y_1,t}^{\mathrm{EV}} P_{e,i}^{\mathrm{EV,c,max}} \tag{70}$$

$$SOC_{e,i}^{\mathrm{EV,min}} \leq \sum_{t'=t_0}^{t} \left(\frac{P_{e,i,t}^{\mathrm{EV,c}} \eta_{e,i}^{\mathrm{EV,c}}}{E_{e,i}^{\mathrm{EV,cap}}} - \frac{P_{e,y_2,t}^{\mathrm{EV,d}}}{E_{e,i}^{\mathrm{EV,cap}}} \right) + SOC_{e,i,t_0}^{\mathrm{EV}} + b_{e,y_2} \sum_{t'=t_0}^{t} \frac{P_{e,y_2,t}^{\mathrm{EV,d}}}{E_{e,i}^{\mathrm{EV,cap}}} \tag{71}$$

$$\sum_{t'=t_0}^{t} \left(\frac{P_{e,i,t}^{\mathrm{EV,c}} \eta_{e,i}^{\mathrm{EV,c}}}{E_{e,i}^{\mathrm{EV,cap}}} - \frac{P_{e,y_2,t}^{\mathrm{EV,d}}}{E_{e,i}^{\mathrm{EV,cap}}} \right) + SOC_{e,i,t_0}^{\mathrm{EV}} \leq SOC_{e,i}^{\mathrm{EV,max}} + b_{e,y_2} \sum_{t'=t_0}^{t} \left(\frac{P_{e,i}^{\mathrm{EV,c,max}}}{E_{e,i}^{\mathrm{EV,cap}}} - \frac{P_{e,y_2,t}^{\mathrm{EV,d}}}{E_{e,i}^{\mathrm{EV,cap}}} \right) \tag{72}$$

$$P_{e,i,t}^{\mathrm{EV,c}} \leq b_{e,y_2,t}^{\mathrm{EV}} P_{e,i}^{\mathrm{EV,c,max}} + b_{e,y_2} P_{e,i}^{\mathrm{EV,c,max}} \tag{73}$$

$$\sum_{y_2 \in \mathcal{Y}_{e,i}^{-}} (\psi_{e,y_2} b_{e,y_2}) \leq 1 - \beta \tag{74}$$

In (68)–(70), the realization y_1 for the driving pattern is satisfied in the original charging constraints (13)–(15). When $b_{e,y_2} = 0$, the realization y_2 for the driving pattern is satisfied in constraints (71)–(73). Constraint (74) guarantees that the failure probability of the realization is below the error level $1 - \beta$. In summary, the original constraints (13)–(15) for EV charging can be replaced by (68)–(74) along with the lower limit for the EV charging in (15) (i.e., $P_{e,i,t}^{\mathrm{EV,c}} \geq 0$).

IV. SIMULATION RESULTS

A. SIMULATION SETUP

We quantified the performance of the proposed approach in the modified IEEE 33-node test feeder [17], as shown in Fig. 3. The test feeder operates at 12.66 kV with 3715 kW and 2300 kVAr of active and reactive power loads, respectively. The maximum and minimum limits of the allowed voltage range were set to $V^{\max} = 1.1$ and $V^{\min} = 0.9$, respectively. The OLTC was connected to the substation, and the tap position of the OLTC ranged from -16 to 16 with a step change $a^{\text{OLTC}} = 0.00625$. The six CBs were installed at nodes 6, 12, 18, 21, 25, and 33, and $Q_i^{\text{CB,nom}}$ was set to 100 kVAr. The stand-alone PV systems were connected to nodes 6 and 18. Fig. 4 presents the profile of the predicted coefficients for PV power generation output and load. The two smart EVCSs equipped with the PV system and ESS were connected to nodes 22 and 23. The capacities for the apparent and reactive powers of the stand-alone PV system and the PV system integrated in the EVCS were identically set to $S_i^{\text{PV,max}} = 500$ kVA and $Q_i^{\text{PV,max}} = 500$ kVAr, respectively. The capacities for the apparent and reactive powers of the EVCS were set to $S_i^{\text{EVCS,max}} = 500$ kVA and $S_i^{\text{EVCS,max}} = 500$ kVAr, respectively. For the ESS in each EVCS, the battery capacity was set to $E_i^{\text{ESS,cap}} = 500$ kWh, and the maximum and minimum charging power of the ESS were both 100 kW. The maximum, minimum, and initial SOC of the ESS were set to $SOC_i^{\text{ESS,max}} = 1$, $SOC_i^{\text{ESS,min}} = 0.2$, and $SOC_{i,t_0}^{\text{ESS}} = 0.5$, respectively. The charging and discharging efficiencies $\eta_i^{\text{ESS,c}}$ and $\eta_i^{\text{ESS,d}}$ of the ESS were set to 0.95. We assumed that each EVCS charged 10 EVs featuring the same specification defined next. The battery capacity of the EV was set to $E_{e,i}^{\text{EV,cap}} = 60$ kWh, whereas the maximum charging power $P_{e,i}^{\text{EV,c,max}}$ of the EV was set to 10 kW. The maximum, minimum, and initial SOC of the EV were set to $SOC_{e,i}^{\text{EV,max}} = 1$, $SOC_{e,i}^{\text{EV,min}} = 0.2$, and $SOC_{e,i,t_0}^{\text{EV}} = 0.2$, respectively. The charging efficiency $\eta_{e,i}^{\text{EV,c}}$ was 0.95. The step size v^{step} in (35)–(38), which determines the incremental voltage step of the Q-V curve, was set to 1. Table 1 includes 10 probabilistic driving patterns of EVs. Based on the results in this table, each EV consumes 150 Wh/km during the trip between the start and end times. The power consumption $P_{e,i,t}^{\text{EV,d}}$ for EV e at EVCS i and time t in (13) is calculated as follows:

$$P_{e,i,t}^{\text{EV,d}} = \frac{\text{Energy consumption per km} \times \text{Driving distance}}{\text{Ending time} - \text{Starting time}}. \tag{75}$$

Initially, the weights ω_1 and ω_2 in the objective function (1) for the proposed VVO problem were set to 0.7 and 0.3, respectively.

Table 2 classifies our simulation study in a total of eight cases. Case1, including Cases1-1∼1-4, represents VVO using the Q-V curve with fixed parameters (i.e., $V_3^{\text{q}} = 0.96$ p.u.

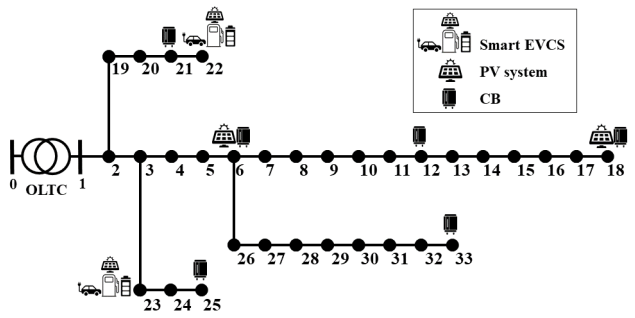

FIGURE 3. Modified IEEE 33-node test feeder.

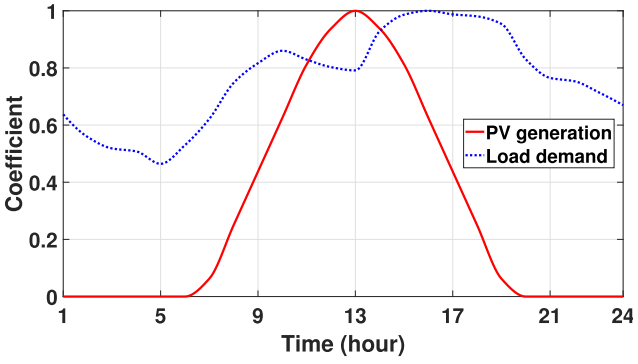

FIGURE 4. Predicted coefficients for PV power generation output and load.

TABLE 1. Probabilistic driving patterns for EVs [38].

Scenario	Starting time	Ending time	Driving distance	Probability
1	4	23	140 km	0.00169
2	4	24	140 km	0.00003
3	5	23	140 km	0.71116
4	5	24	140 km	0.03383
5	4	23	150 km	0.00008
6	5	23	150 km	0.00671
7	5	24	150 km	0.00049
8	4	23	160 km	0.00032
9	5	23	160 km	0.04367
10	5	24	160 km	0.00506

TABLE 2. Classification for case studies.

Cases	Optimized Q-V curve	PV uncertainty	EV uncertainty
Case1-1	✗	✗	✗
Case1-2	✗	✓	✗
Case1-3	✗	✗	✓
Case1-4	✗	✓	✓
Case2-1	✓	✗	✗
Case2-2	✓	✓	✗
Case2-3	✓	✗	✓
Case2-4	✓	✓	✓

TABLE 3. Active power loss (MW) in the IEEE 33-node test feeder throughout the day for all cases.

Cases	DO	CCO		
		$\beta = 0.68$	$\beta = 0.85$	$\beta = 0.95$
Case1-1	1.6296	-	-	-
Case1-2	-	1.6330	1.6337	1.6366
Case1-3	-	1.6308	1.6310	1.6312
Case1-4	-	1.6335	1.6342	1.6371
Case2-1	1.4962	-	-	-
Case2-2	-	1.4962	1.5001	1.5100
Case2-3	-	1.4964	1.4977	1.4997
Case2-4	-	1.4970	1.5156	1.5162

and $V_3^{\mathrm{q}} = 1.04$ p.u.), whereas Case2, including Cases2-1∼2-4, represents VVO using the optimized Q-V curve with adjusted parameters ($V_{i,3}^{\mathrm{q}}$ and $V_{i,4}^{\mathrm{q}}$). Case1 and Case2 are divided into four subcases according to the existence of PV and EV uncertainties. In cases without EV uncertainty, the EV driving pattern was selected as scenario 3 from Table 1. The mean and standard deviation of the prediction error $P_{i,t}^{\mathrm{PV,err}}$ of the PV generation output were set to $\mu_{i,t}^{\mathrm{PV,err}} = 0$ and $\sigma_{i,t}^{\mathrm{PV,err}} = 0.15$, respectively. Three probability levels in the chance constraints were selected as $\beta = 0.68,\ 0.85$, and 0.95. The simulation study was conducted in MATLAB 2020a with the CPLEX optimization solver 12.10.

B. PERFORMANCE ASSESSMENT OF THE PROPOSED APPROACH

1) IMPACT OF OPTIMIZED Q-V CURVE AND PV UNCERTAINTY ON VVO RESULTS

Table 3 presents the results of total active power loss for all nodes throughout the day in eight cases. In this subsection, we consider cases without EV uncertainty (i.e., Cases1-1, 1-2, 2-1, and 2-2). Note from Table 3 that Case2-1 yields less active power loss than Case1-1; the relative reduction of the active power loss in Case2-1 to Case1-1 is 8.1861%. In addition, for three different values of β, the active power losses in Case2-2 are smaller than those in Case1-2, and the relative reductions in the active power losses in Case2-2 to Case1-2 are 8.1384%, 7.5718%, and 7.3995%, respectively, corresponding to $\beta = 0.68,\ 0.85$ and 0.95. The aforementioned observations demonstrate that VVO using the optimized Q-V curve can further reduce the active power loss compared to VVO using the Q-V curve with fixed parameters. Another observation from Table 3 is that the CCO approach results in an increasing active power loss as the probability level β increases. This is because the chance constraints related to the probability level become further constricted and the feasible region of the CCO problem becomes narrower with an increasing probability level, thereby increasing the value of the objective function in the CCO problem.

Table 4 presents the results for the minimum and maximum voltage magnitudes for all nodes throughout the day

TABLE 4. Maximum and minimum voltage magnitude (p.u.) in the IEEE 33-node test feeder throughout the day for all cases.

Cases	Voltage	DO	CCO		
			$\beta = 0.68$	$\beta = 0.85$	$\beta = 0.95$
Case1-1	$\min(V_{i,t})$	0.9494	-	-	-
	$\max(V_{i,t})$	1.0321	-	-	-
Case1-2	$\min(V_{i,t})$	-	0.9497	0.9490	0.9495
	$\max(V_{i,t})$	-	1.0272	1.0325	1.0326
Case1-3	$\min(V_{i,t})$	-	0.9497	0.9490	0.9490
	$\max(V_{i,t})$	-	1.0188	1.0260	1.0260
Case1-4	$\min(V_{i,t})$	-	0.9497	0.9494	0.9493
	$\max(V_{i,t})$	-	1.0437	1.0314	1.0248
Case2-1	$\min(V_{i,t})$	0.9464	-	-	-
	$\max(V_{i,t})$	1.0500	-	-	-
Case2-2	$\min(V_{i,t})$	-	0.9501	0.9502	0.9499
	$\max(V_{i,t})$	-	1.0501	1.0500	1.0501
Case2-3	$\min(V_{i,t})$	-	0.9500	0.9495	0.9503
	$\max(V_{i,t})$	-	1.0562	1.0517	1.0500
Case2-4	$\min(V_{i,t})$	-	0.9501	0.9502	0.9499
	$\max(V_{i,t})$	-	1.0501	1.0500	1.0501

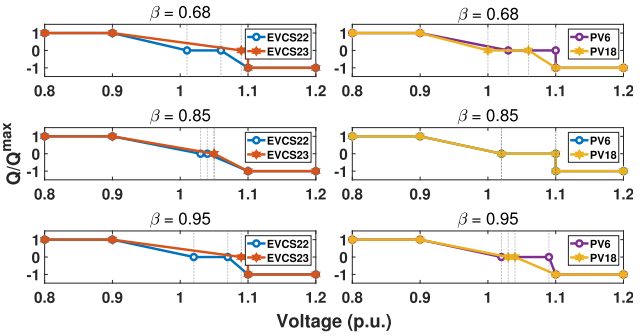

FIGURE 5. Q-V curves of EVCSs and PV systems in Case2-2 with varying β.

in eight cases. From this table, we verify that the minimum and maximum voltage magnitudes for Cases2-1 and 2-2 using the optimized Q-V curves are higher than the minimum and maximum voltage magnitudes for Cases1-1 and 1-2 using the fixed Q-V curves. This is because a trade-off relationship exists between the active power loss and voltage magnitude. That is, given the fixed apparent power, a higher voltage magnitude owing to an increasing β generally leads to a lower current magnitude and subsequent decreasing active power loss, which is consistent with the results in Table 3.

Fig. 5 shows the results of the optimized Q-V curves for the smart inverters of two PV systems and EVCSs in Case2-2 with varying β. Using the optimized Q-V curves along with the local voltage measurements, the smart inverters dynamically adjust their reactive power; they provide reactive power to increase the voltage when the voltage is lower than the minimum limit of the dead band of the Q-V curve, and absorb reactive power when the voltage is higher than the maximum limit of the dead band of the Q-V curve. Note from Fig. 5 that the dead bands for all Q-V curves are shifted to a higher voltage range than 1 p.u. This is because most of the nodal voltages are below 1 p.u., as shown in Fig. 6, in which the smart inverters aim to prevent voltage violation

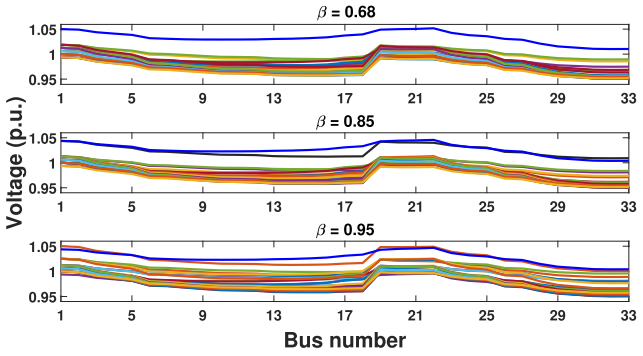

FIGURE 6. Voltage profile for 33 nodes during 24 h in Case2-2 with varying β.

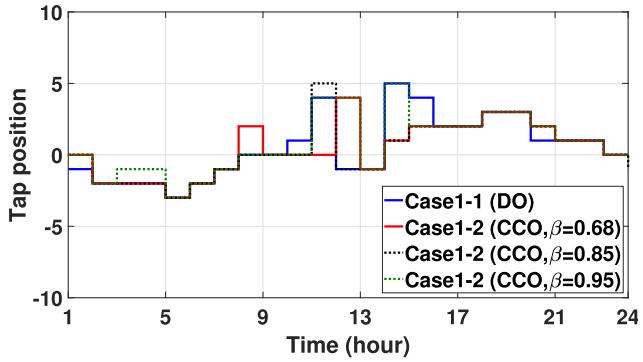

FIGURE 7. Tap positions of the OLTC during 24 h in Cases1-1 and 1-2 with varying β.

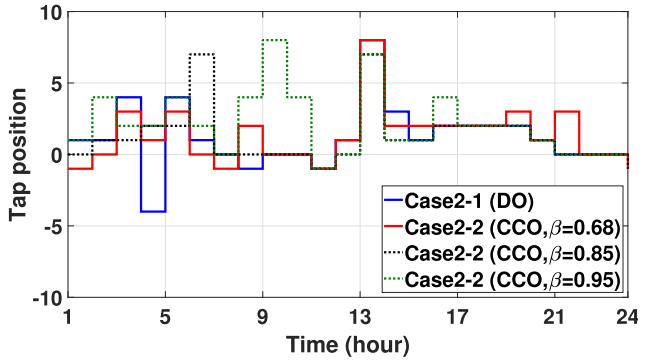

FIGURE 8. Tap positions of the OLTC during 24 h in Cases2-1 and 2-2 with varying β.

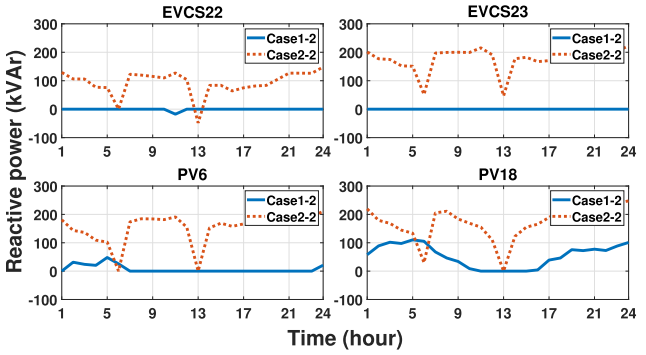

FIGURE 9. Reactive power dispatch of EVCSs and PV systems during 24 h in Cases1-2 and 2-2 with $\beta = 0.85$.

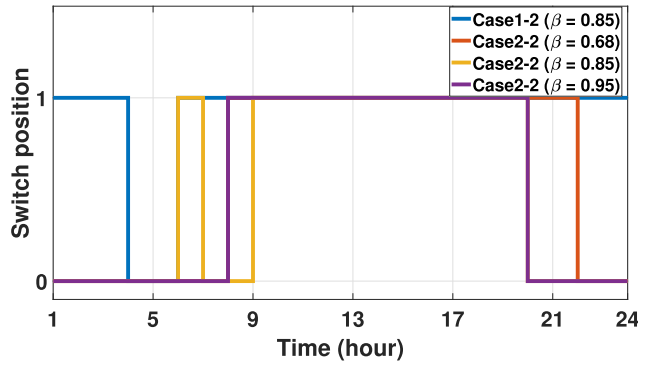

FIGURE 10. Switch positions of CB18 during 24 h in Cases1-2 and 2-2.

at its minimum limit by supplying reactive power to the grid more frequently than absorbing reactive power from the grid.

Figs. 7 and 8 show the OLTC tap positions for Cases1-1, 1-2, and Cases2-1, 2-2, respectively. We can see from the comparison of Figs. 7 and 8 that, in general, the OLTC tap positions for Cases2-1 and 2-2 ($-3 \leq Tap_t^{\mathrm{OLTC}} \leq 5$) fluctuate more than for Cases1-1 and 1-2 ($-4 \leq Tap_t^{\mathrm{OLTC}} \leq 8$). We conjecture from this phenomenon that the optimized Q-V curves enable the OLTC to operate more actively for minimizing the total active power loss while maintaining an acceptable voltage level.

Fig. 9 depicts the reactive power of two EVCSs and PV systems for Cases1-2 and 2-2 with $\beta = 0.85$. Note from this figure that the smart inverters in Case2-2 inject more reactive power into the grid than the smart inverters in Case1-2. This demonstrates that the optimized Q-V curves with higher dead bands than the fixed Q-V curves enable the smart inverters to further supply reactive power to the grid to maintain a stable grid operation. In addition, it can be observed from Fig. 9 that the optimized Q-V curve-based smart inverter for EVCS23 supplies reactive power to the grid without absorbing the reactive power from the grid during the day. This is because the ESS in EVCS23 reduces the active power consumption of EVCS23 through the discharging process, thereby increasing the capability of the reactive power support for the smart inverter of the EVCS23.

Figs. 10 and 11 show the switch positions for CB18 and CB21 in Cases1-2 and 2-2, respectively. In the simulation, the switches of other four CBs (CB6, CB12, CB25, and CB33) always turn on for 24 h. Compared to the switch positions of these four CBs, it can be observed from Figs. 10 and 11 that CB18 and CB21 are frequently switched on and off during 24 h. This observation derives from the fact that the nodes 18 and 21 equipped with CB18 and CB21 are

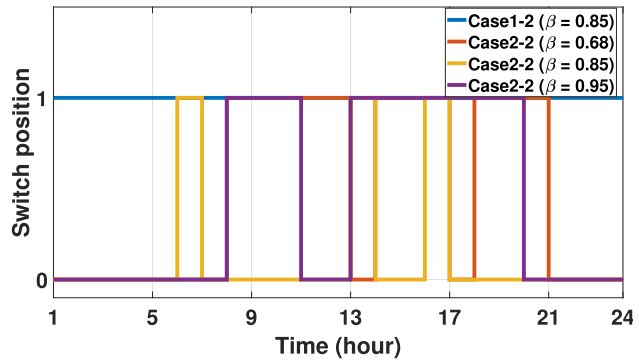

FIGURE 11. Switch positions of CB21 during 24 h in Cases1-2 and 2-2.

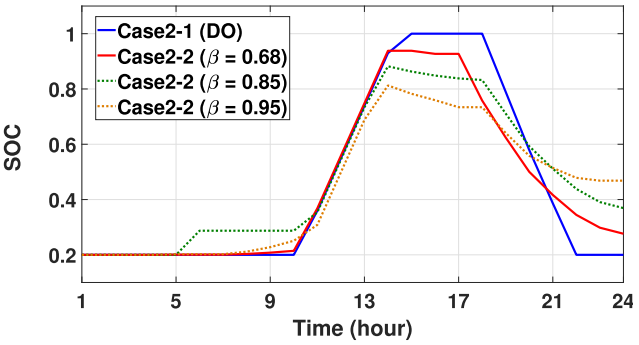

FIGURE 12. SOC of ESS23 during 24 h in Cases2-1 and 2-2 with varying β.

i) almost end nodes of the test system, in which the CBs dynamically operate to maintain an acceptable voltage level, and ii) nodes adjacent to the PV system and EVCS, whose inverters significantly inject or absorb reactive power, which in turn leads to the frequent change in the switch positions of the CBs.

Fig. 12 compares the SOC results of ESS23 in Cases2-1 and 2-2 with varying β. Note from this figure that the values of the SOC remain at their minimum limit during the time period [12:00 a.m., 5:00 a.m.] because ESS23 discharges power to the EVs connected to EVCS23 at this time period. After 5:00 a.m., the SOCs gradually increase as the EVCS load and PV generation output increase as shown in Fig. 4. Approximately 10:00 a.m., the EVCS load decreases, whereas the PV generation output increases, thereby leading to a sharp increase in the SOCs. Then, the level of the SOC reaches its maximum approximately 2:00 p.m. owing to the charging, with significant increase of the PV generation output. Afterwards, the level of the SOC decreases while the ESS supports the load demand of the EVCS. Another observation from Fig. 12 is that the upper bound of SOC in Case2-1 is larger than in Case2-2. This is because the CCO approach (Case2-2) yields a more conservative solution under uncertainty than the DO approach (Case2-1). In addition, in Case2-2, note that an increasing probability level β results in a decreasing upper bound of the SOC because the limits of chance constraints associated with the SOC are further constricted. As shown in the results shown in Table 3, a more restricted charging capability of the ESS owing to a higher β leads to an increase in the active power loss.

2) IMPACT OF OPTIMIZED Q-V CURVE AND EV UNCERTAINTY ON VVO RESULTS

In this subsection, we consider cases with EV uncertainty for Cases1-3 and 1-4 using the fixed Q-V curves and Cases2-3 and 2-4 using the optimized Q-V curves. Similar to the results in Section IV-B1, Table 3 shows that Cases2-3 and 2-4 result in less active power loss than Cases1-3 and 1-4, respectively, and the relative reductions in the active power losses for Cases2-3 and 2-4 with respect to Cases1-3 and 1-4 under different $\beta = 0.68,\ 0.85$ and 0.95 are calculated as $\{8.9815\%, 8.9\%, 8.7684\%\}$ and $\{9.1182\%, 7.8252\%, 7.9738\%\}$, respectively. In addition, note from Table 4 that Cases2-3 and 2-4 yield higher minimum and maximum voltage magnitudes than Cases1-1 and 1-2. Based on the aforementioned observations, we conclude that the optimized Q-V curves under PV uncertainty and/or EV uncertainty can successfully reduce the total active power loss at the expense of increasing voltage magnitudes.

Fig. 13 shows the EV charging schedules at the time period [1 a.m., 5 a.m.] for Case2-1 and Case2-4 with varying β. In this figure, EV1∼EV10 and EV11∼EV20 charge at EVCS22 and EVCS23, respectively. Note from Case2-4 in Fig. 13 that, in general, the number of charging EVs and their charging power increase as the probability level β increases. This phenomenon is due to the fact that an increasing β leads to a larger number of realizations for the EV driving patterns, thereby providing the EVCS with the capability of flexible adaptation to the EV charging demand. A higher charging power from the EVCS owing to a higher β yields a greater active power loss, which is verified in Cases2-3 and 2-4 in Table 3.

Fig. 14 shows the results of the Q-V curves for the smart inverters of two PV systems and EVCSs in Case2-4 with varying β. A similar phenomenon shown in Fig. 5, in which only the PV uncertainty is considered, is observed in Fig. 14, which considers both PV and EV uncertainties; the dead bands for all Q-V curves are shifted to a voltage higher than 1 p.u. We conjecture that a higher EV uncertainty leads to a voltage violation at its minimum limit with decreasing voltage owing to a larger EV charging demand, thereby enabling the smart inverters to supply more reactive power to the grid to mitigate such voltage violation.

3) IMPACT OF DIFFERENT WEIGHTS IN THE OBJECTIVE FUNCTION ON VVO RESULTS

Table 5 shows the results of the total active power loss and voltage deviation in terms of weights ω_1 and ω_2 in the objective function of the VVO problem. As expected, the results show a trade-off relationship between the total active power loss and voltage deviation according to changes in ω_1 and

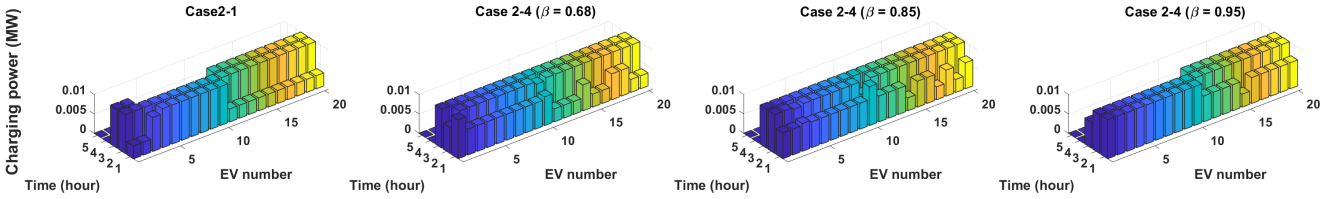

FIGURE 13. EV charging schedules between 1 a.m. and 5 a.m. in Cases2-1 and 2-4 with varying β.

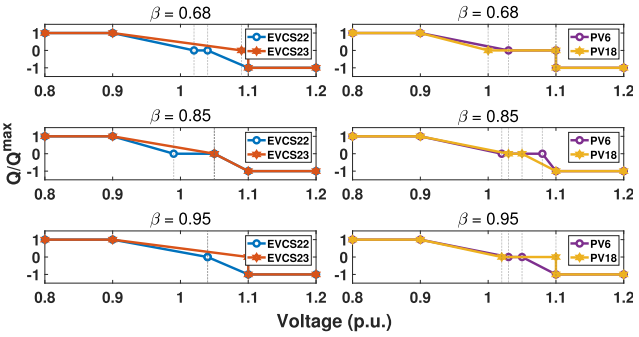

FIGURE 14. Q-V curves of EVCSs and PV systems in Case2-4 with varying β.

TABLE 5. Results with varying weights in the objective function of the proposed VVO model.

ω_1	ω_2	Category	$\beta = 0.68$	$\beta = 0.85$	$\beta = 0.95$
0.9	0.1	$\sum_{t\in\mathcal{T}}\sum_{ij\in\mathcal{L}} P^{\text{loss}}_{ij,t}$	1.4932	1.5026	1.5054
		$\sum_{t\in\mathcal{T}}\sum_{i\in\mathcal{N}} \Delta V_{i,t}$	0.01529	0.00689	0.02373
0.7	0.3	$\sum_{t\in\mathcal{T}}\sum_{ij\in\mathcal{L}} P^{\text{loss}}_{ij,t}$	1.4970	1.5156	1.5162
		$\sum_{t\in\mathcal{T}}\sum_{i\in\mathcal{N}} \Delta V_{i,t}$	0.00011	0	0.00024
0.5	0.5	$\sum_{t\in\mathcal{T}}\sum_{ij\in\mathcal{L}} P^{\text{loss}}_{ij,t}$	1.5080	1.5170	1.5182
		$\sum_{t\in\mathcal{T}}\sum_{i\in\mathcal{N}} \Delta V_{i,t}$	0.00005	0	0.00010

ω_2. As shown in Table 5, a higher (or lower) ω_1 leads to a lower (or higher) total active power loss, whereas a higher (or lower) ω_2 leads to a lower (or higher) total voltage deviation. Based on this trade-off relationship, system operators may adaptively adjust the weights ω_1 and ω_2 to situations in which they aim to further reduce the active power loss or maintain better voltage quality.

C. SCALABILITY

To verify the scalability of the proposed algorithm, the performance of the proposed algorithm was assessed in the IEEE 69-node test feeder [39]. The test feeder operates at 12.66 kV with 3802 kW and 2695 kVAr of active and reactive power loads, respectively. The six CBs were installed at nodes 6, 22, 34, 40, 60, and 69. The stand-alone PV systems were connected to nodes 7 and 27 and two smart EVCSs with the PV system and ESS were connected to nodes 35 and 65. The weights ω_1 and ω_2 in the objective function were set to $\omega_1 = 0.7$ and $\omega_2 = 0.3$, respectively. For the sake of simplicity, the values of other parameters in the IEEE 69-node test feeder are the same as those in the IEEE 33-node test feeder.

TABLE 6. Active power loss (MW) in the IEEE 69-node test feeder for Cases1-4 and 2-4.

Cases	Active power loss (MW)		
	$\beta = 0.68$	$\beta = 0.85$	$\beta = 0.95$
Case1-4	1.5897	1.6006	1.6123
Case2-4	1.4606	1.4720	1.4898

TABLE 7. Comparison of computation time (s) of the proposed algorithm between the IEEE 33-node and IEEE 69-node feeders for Case2-4.

Test system	Computation time (s)		
	$\beta = 0.68$	$\beta = 0.85$	$\beta = 0.95$
IEEE 33-node	263.3	271.8	199.9
IEEE 69-node	640.53	349.8	620.6

Table 6 compares the results of the total active power loss in terms of β between Case1-4 and Case2-4. Similar to the result in the IEEE 33-node test feeder, we verify from this table that Case2-4 yields less active power loss than Case 1-4 under different β. The relative reduction of the active power loss in Case2-4 to Case1-4 are 8.1210%, 8.0345%, and 7.598%, respectively, corresponding to $\beta = 0.68$, 0.85, and 0.95.

Table 7 compares the computation time of the proposed approach between the IEEE 33-node and IEEE 69-node feeders for Case2-4 under different β. As expected, this table shows that the computation time increases as the size of the test system becomes larger. Note that these computation times in Table 7 can be acceptable because the proposed approach conducts day-ahead scheduling with one-hour resolution.

Finally, the novelty of the proposed approach and meaningful observations from the simulation study can be summarized as follows:

- Compared to existing hierarchical VVO methods, which did not consider the voltage regulation capability of smart EVCSs under uncertainties of the PV generation output and EV driving pattern, the proposed hierarchical VVO approach reflects the voltage control of smart EVCSs in both the global and local control stages, which are integrated with the optimized Q-V curves for smart inverters of PV systems and smart EVCSs.
- The results in Tables 3 and 4 show that the optimized Q-V curves (Cases2-1∼Cases2-4) for the smart inverters of the PV system and EVCS significantly reduce the

total active power loss compared to the fixed Q-V curves (Cases1-1∼Cases1-4) at the cost of increasing the maximum and minimum voltage magnitudes.
- In contrast with the DO-based VVO approach, the CCO-based VVO approach improves the robustness of the PV generation output and EV driving pattern against uncertainties at the cost of increasing the total active power loss and maximum/minimum voltage magnitude.
- In the CCO-based VVO approach, an increasing probability level β in the chance constraints leads to a larger total active power loss and maximum/minimum voltage magnitude owing to a further restriction of the reactive power capability of the smart inverters while maintaining the robustness of the CCO-based VVO approach against uncertainty.

V. CONCLUSION

This study proposes a hierarchical framework to conduct the VVO process that involves global and local voltage controls of smart EVCSs integrated with PV systems and ESSs. In the proposed framework, the total active power loss and voltage violation can be minimized at the global control stage through i) the coordination of the smart inverters of the EVCSs and PV systems and conventional voltage regulators, and ii) parameter adjustment for the Q-V curves of the smart inverters of the EVCSs and PV systems. At the local control stage, the Q-V curves optimized at the global control stage are exploited by the smart inverters to rapidly mitigate local voltage violations owing to intermittent PV generation output. To incorporate the uncertainties in PV generation outputs and driving patterns of EV users into the proposed framework, the DO-based VVO problem at the global control stage was reformulated into the CCO-based VVO problem with probability constraints. The simulation results show that, compared to the VVO framework with fixed Q-V curves, the proposed framework based on the optimized Q-V curves can successfully reduce the total active power loss and voltage deviation. Furthermore, the robustness of the CCO-based VVO problem against uncertainties in PV generation outputs and driving patterns of EV users was verified with varying probability levels of chance constraints.

The proposed VVO framework at the global control stage is implemented in a centralized manner, which may significantly increase the computational complexity in larger power distribution networks with various DERs. In future studies, the centralized DO- and CCO-based VVO approaches will be extended to the distributed VVO approaches that include the global and local voltage control capability of smart EVCSs, and a performance comparison between the centralized and distributed VVO approaches will be conducted in large power distribution systems.

REFERENCES

[1] P. Wirasanti, E. Ortjohann, M. Hoppe, H. Saffour, S. Leksawat, and D. Morton, "Automated active distribution network with multi-level cluster control approach," in *Proc. 39th Annu. Conf. IEEE Ind. Electron. Soc. (IECON)*, Nov. 2013, pp. 1980–1985, doi: 10.1109/iecon.2013.6699435.

[2] A. Ipakchi and F. Albuyeh, "Grid of the future," *IEEE Power Energy Mag.*, vol. 7, no. 2, pp. 52–62, , Mar. 2009, doi: 10.1109/mpe.2008.931384.

[3] V. Agarwal and L. H. Tsoukalas, "Smart grids: Importance of power quality," in *Energy-Efficient Computing and Networking*, N. Hatziargyriou, A. Dimeas, T. Tomtsi, and A. Weidlich, Eds. Berlin, Germany: Springer, 2011, pp. 136–143.

[4] S. A. Arefifar, Y. A.-R. I. Mohamed, and T. H. M. El-Fouly, "Comprehensive operational planning framework for self-healing control actions in smart distribution grids," *IEEE Trans. Power Syst.*, vol. 28, no. 4, pp. 4192–4200, Nov. 2013, doi: 10.1109/tpwrs.2013.2259852.

[5] K. Samarakoon, J. Ekanayake, and N. Jenkins, "Reporting available demand response," *IEEE Trans. Smart Grid*, vol. 4, no. 4, pp. 1842–1851, Dec. 2013, doi: 10.1109/tsg.2013.2258045.

[6] B. Wang, M. Sechilariu, and F. Locment, "Intelligent DC microgrid with smart grid communications: Control strategy consideration and design," *IEEE Trans. Smart Grid*, vol. 3, no. 4, pp. 2148–2156, Dec. 2012, doi: 10.1109/tsg.2012.2217764.

[7] M. Pilz and L. Al-Fagih, "Recent advances in local energy trading in the smart grid based on game-theoretic approaches," *IEEE Trans. Smart Grid*, vol. 10, no. 2, pp. 1363–1371, Mar. 2019, doi: 10.1109/tsg.2017.2764275.

[8] H. Haghighat, H. Karimianfard, and B. Zeng, "Integrating energy management of autonomous smart grids in electricity market operation," *IEEE Trans. Smart Grid*, vol. 11, no. 5, pp. 4044–4055, Sep. 2020, doi: 10.1109/tsg.2020.2992570.

[9] K. Kuroda, H. Magori, T. Ichimura, and R. Yokoyama, "A hybrid multi-objective optimization method considering optimization problems in power distribution systems," *J. Mod. Power Syst. Clean Energy*, vol. 3, no. 1, pp. 41–50, Jan. 2015, doi: 10.1007/s40565-015-0096-0.

[10] C. K. Das, O. Bass, G. Kothapalli, T. S. Mahmoud, and D. Habibi, "Optimal placement of distributed energy storage systems in distribution networks using artificial bee colony algorithm," *Appl. Energy*, vol. 232, pp. 212–228, Dec. 2018, doi: 10.1016/j.apenergy.2018.07.100.

[11] R. K. Varma and E. M. Siavashi, "PV-STATCOM: A new smart inverter for voltage control in distribution systems," *IEEE Trans. Sustain. Energy*, vol. 9, no. 4, pp. 1681–1691, Oct. 2018, doi: 10.1109/TSTE.2018.2808601.

[12] Z. Wang, J. Wang, B. Chen, M. M. Begovic, and Y. He, "MPC-based voltage/VAR optimization for distribution circuits with distributed generators and exponential load models," *IEEE Trans. Smart Grid*, vol. 5, no. 5, pp. 2412–2420, Sep. 2014, doi: 10.1109/TSG.2014.2329842.

[13] S. M. N. R. Abadi, P. Scott, and S. Thiebaux, "A combined central-local volt/VAR approach in distribution systems with high PV uptake," in *Proc. Int. Conf. Smart Grids Energy Syst. (SGES)*, Nov. 2020, pp. 606–611, doi: 10.1109/SGES51519.2020.00113.

[14] M. Boucher, "Transportation electrification and managing traffic congestion: The role of intelligent transportation systems," *IEEE Electrific. Mag.*, vol. 7, no. 3, pp. 16–22, Sep. 2019, doi: 10.1109/MELE.2019.2925730.

[15] W. Lee, L. Xiang, R. Schober, and V. W. S. Wong, "Electric vehicle charging stations with renewable power generators: A game theoretical analysis," *IEEE Trans. Smart Grid*, vol. 6, no. 2, pp. 608–617, Mar. 2015, doi: 10.1109/tsg.2014.2374592.

[16] U. Datta, A. Kalam, and J. Shi, "Smart control of bess in PV integrated EV charging station for reducing transformer overloading and providing battery-to-grid service," *J. Energy Storage*, vol. 28, Apr. 2020, Art. no. 101224, doi: 10.1016/j.est.2020.101224.

[17] M. E. Baran and M.-Y. Hsu, "Volt/VAR control at distribution substations," *IEEE Trans. Power Syst.*, vol. 14, no. 1, pp. 312–318, Feb. 1999, doi: 10.1109/59.744549.

[18] H. Ahmadi, J. R. Martí, and H. W. Dommel, "A framework for volt-VAR optimization in distribution systems," *IEEE Trans. Smart Grid*, vol. 6, no. 3, pp. 1473–1483, May 2015, doi: 10.1109/tsg.2014.2374613.

[19] S. Auchariyamet and S. Sirisumrannukul, "Optimal dispatch of ULTC and capacitors for volt/VAR control in distribution system with harmonic consideration by particle swarm approach," in *Proc. Int. Conf. Sustain. Power Gener. Supply*, Apr. 2009, pp. 1–7, doi: 10.1109/supergen.2009.5348357.

[20] A. Padilha-Feltrin, D. A. Q. Rodezno, and J. R. S. Mantovani, "Volt-VAR multiobjective optimization to peak-load relief and energy efficiency in distribution networks," *IEEE Trans. Power Del.*, vol. 30, no. 2, pp. 618–626, Apr. 2015, doi: 10.1109/tpwrd.2014.2336598.

[21] R. R. Jha, A. Dubey, C.-C. Liu, and K. P. Schneider, "Bi-level volt-VAR optimization to coordinate smart inverters with voltage control devices," *IEEE Trans. Power Syst.*, vol. 34, no. 3, pp. 1801–1813, May 2019, doi: 10.1109/tpwrs.2018.2890613.

[22] R. A. Jabr, "Robust volt/VAR control with photovoltaics," *IEEE Trans. Power Syst.*, vol. 34, no. 3, pp. 2401–2408, May 2019, doi: 10.1109/tpwrs.2018.2890767.
[23] F. U. Nazir, B. C. Pal, and R. A. Jabr, "A two-stage chance constrained volt/VAR control scheme for active distribution networks with nodal power uncertainties," *IEEE Trans. Power Syst.*, vol. 34, no. 1, pp. 314–325, Jan. 2019, doi: 10.1109/tpwrs.2018.2859759.
[24] D. Mak and D.-H. Choi, "Optimization framework for coordinated operation of home energy management system and volt-VAR optimization in unbalanced active distribution networks considering uncertainties," *Appl. Energy*, vol. 276, Oct. 2020, Art. no. 115495, doi: 10.1016/j.apenergy.2020.115495.
[25] R. Zafar, J. Ravishankar, J. E. Fletcher, and H. R. Pota, "Optimal dispatch of battery energy storage system using convex relaxations in unbalanced distribution grids," *IEEE Trans. Ind. Informat.*, vol. 16, no. 1, pp. 97–108, Jan. 2020, doi: 10.1109/tii.2019.2912925.
[26] L. H. Macedo, J. F. Franco, M. J. Rider, and R. Romero, "Optimal operation of distribution networks considering energy storage devices," *IEEE Trans. Smart Grid*, vol. 6, no. 6, pp. 2825–2836, Nov. 2015, doi: 10.1109/tsg.2015.2419134.
[27] B. Zhang, A. Y. S. Lam, A. Domínguez-García, and D. Tse, "An optimal and distributed method for voltage regulation in power distribution systems," *IEEE Trans. Power Syst.*, vol. 30, no. 4, pp. 1714–1726, Jul. 2015, doi: 10.1109/tpwrs.2014.2347281.
[28] Y. Zheng, Y. Song, D. J. Hill, and K. Meng, "Online distributed MPC-based optimal scheduling for EV charging stations in distribution systems," *IEEE Trans. Ind. Informat.*, vol. 15, no. 2, pp. 638–649, Feb. 2019, doi: 10.1109/tii.2018.2812755.
[29] A. O'Connell and A. Keane, "Volt-VAR curves for photovoltaic inverters in distribution systems," *IET Gener., Transmiss. Distrib.*, vol. 11, no. 3, pp. 730–739, Feb. 2017, doi: 10.1049/iet-gtd.2016.0409.
[30] C. Zhang, Y. Xu, Z. Dong, and J. Ravishankar, "Three-stage robust inverter-based voltage/VAR control for distribution networks with high-level PV," *IEEE Trans. Smart Grid*, vol. 10, no. 1, pp. 782–793, Jan. 2019, doi: 10.1109/TSG.2017.2752234.
[31] D. Mak and D.-H. Choi, "Hierarchical look-ahead conservation voltage reduction framework considering distributed energy resources and demand reduction," *Energies*, vol. 11, no. 12, p. 3250, Nov. 2018, doi: 10.3390/en11123250.
[32] L. Wang, R. Yan, and T. K. Saha, "Voltage management for large scale PV integration into weak distribution systems," *IEEE Trans. Smart Grid*, vol. 9, no. 5, pp. 4128–4139, Sep. 2018, doi: 10.1109/TSG.2017.2651030.
[33] H. Ji, C. Wang, and P. Li, "A centralized-based method to determine the local voltage control strategies of distributed generator operation in active distribution networks," *Appl. Energy*, vol. 228, pp. 2024–2036, Oct. 2018, doi: 10.1016/j.apenergy.2018.07.065.
[34] P. Li, H. Ji, H. Yu, J. Zhao, C. Wang, G. Song, and J. Wu, "Combined decentralized and local voltage control strategy of soft open points in active distribution networks," *Appl. Energy*, vol. 241, pp. 613–624, May 2019, doi: 10.1016/j.apenergy.2019.03.031.
[35] P. Li, J. Ji, H. Ji, J. Jian, F. Ding, J. Wu, and C. Wang, "MPC-based local voltage control strategy of DGs in active distribution networks," *IEEE Trans. Sustain. Energy*, vol. 11, no. 4, pp. 2911–2921, Oct. 2020, doi: 10.1109/TSTE.2020.2981486.
[36] B. Chen, C. Chen, J. Wang, and K. L. Butler-Purry, "Multi-time step service restoration for advanced distribution systems and microgrids," *IEEE Trans. Smart Grid*, vol. 9, no. 6, pp. 6793–6805, Nov. 2018, doi: 10.1109/tsg.2017.2723798.
[37] K. Baker, G. Hug, and X. Li, "Energy storage sizing taking into account forecast uncertainties and receding horizon operation," *IEEE Trans. Sustain. Energy*, vol. 8, no. 1, pp. 331–340, Jan. 2017, doi: 10.1109/tste.2016.2599074.
[38] Z. Liu, Q. Wu, S. S. Oren, S. Huang, R. Li, and L. Cheng, "Distribution locational marginal pricing for optimal electric vehicle charging through chance constrained mixed-integer programming," *IEEE Trans. Smart Grid*, vol. 9, no. 2, pp. 644–654, Mar. 2018, doi: 10.1109/tsg.2016.2559579.
[39] D. Das, "Optimal placement of capacitors in radial distribution system using a fuzzy-GA method," *Int. J. Electr. Power Energy Syst.*, vol. 30, nos. 6–7, pp. 361–367, Jul. 2008.

PANGGAH PRABAWA (Student Member, IEEE) received the B.E. degree in electrical engineering from the Institut Teknologi Sepuluh Nopember, Surabaya, Indonesia, in 2018, and the M.Sc. degree in electrical and electronics engineering from Chung-Ang University, Seoul, South Korea, where he is currently pursuing the Ph.D. degree in electrical and electronics engineering. His current research interests include voltage control and service restoration in power distribution systems.

DAE-HYUN CHOI (Member, IEEE) received the B.S. degree in electrical engineering from Korea University, Seoul, South Korea, in 2002, and the M.Sc. and Ph.D. degrees in electrical and computer engineering from Texas A&M University, College Station, TX, USA, in 2008 and 2014, respectively. From 2002 to 2006, he was a Researcher with Korea Telecom (KT), Seoul, where he worked on designing and implementing home network systems. From 2014 to 2015, he was a Senior Researcher with LG Electronics, Seoul, where he developed home energy management systems. He is currently an Associate Professor with the School of Electrical and Electronics Engineering, Chung-Ang University, Seoul. His research interests include power system state estimation, electricity markets, cyber-physical security of smart grids, and the theory and application of cyber-physical energy systems. He received the Best Paper Award from the 2012 IEEE Third International Conference on Smart Grid Communications (SmartGridComm), Tainan, Taiwan.